International Journal of Pharmaceutics 703 (2026) 127356

Contents lists available at ScienceDirect

International Journal of Pharmaceutics

journal homepage: www.elsevier.com/locate/ijpharm

Exploring alginate/zinc oxide-based 3D-printed structures for application as customizable wound dressings

Sara Cardoso [a,b], Victor Martin [c,d], Catarina Leal [e,f,g], Nuno Monge [h], Bruno Colaço [i,j,k], Pedro Gomes [c,d], Ana F. Bettencourt [a,b], Isabel A.C. Ribeiro [a,b,*]

[a] Research Institute for Medicines (iMed.ULisboa), Faculty of Pharmacy, Universidade de Lisboa, Avenida Prof. Gama Pinto, 1649-003 Lisboa, Portugal
[b] Faculty of Pharmacy, Universidade de Lisboa, Avenida Prof. Gama Pinto, 1649-003 Lisboa, Portugal
[c] BoneLab, Faculdade de Medicina Dentária, Universidade do Porto, Rua Dr. Manuel Pereira da Silva, 4200-393 Porto, Portugal
[d] LAQV/REQUIMTE, Faulddade de Medicina Dentária, Universidade do Porto, Rua Dr. Manuel Pereira da Silva, 4200-393, Porto, Portugal
[e] Departamento de Física, Instituto Superior de Engenharia de Lisboa, Instituto Politécnico de Lisboa 1959-007 Lisboa, Portugal
[f] CENIMAT/I3N, NOVA School of Science and Technology, NOVA University Lisbon, 2829-516 Caparica, Portugal
[g] Centro de Física e Engenharia de Materiais Avançados, Instituto Superior Técnico, Universidade de Lisboa 1049-001 Lisboa, Portugal
[h] Instituto Politécnico de Lisboa, Escola Superior de Educação, ESELx, Campus de Benfica do IPL, Lisboa 1549-003, Portugal
[i] CITAB-Centre for Research and Technology of Agro-Environmental and Biological Sciences, Inov4Agro, University of Trás-os-Montes and Alto Douro, 5000-801 Vila Real, Portugal
[j] CECAV - Animal and Veterinary Research Centre, Associate Laboratory for Animal and Veterinary Sciences (AL4AnimalS), University of Trás-os-Montes and Alto Douro (UTAD), Vila Real, Portugal
[k] Department of Animal Sciences, School of Agrarian and Veterinary Sciences, University of Trás-os-Montes and Alto Douro (UTAD), Vila Real, Portugal

ARTICLE INFO

Keywords:
Wound dressings
Regenerative potential
Infected wounds
3D printing
Polymeric hydrogels

ABSTRACT

Chronic wounds represent a significant global healthcare burden due to the limited effectiveness of current therapeutic strategies. To address this critical need, we developed 3D-printed regenerative wound dressings that can be customized with antimicrobial drugs tailored to individual patient requirements. A novel semisolid extrusion ink combining the biocompatibility and printing properties of alginate (Alg) with the regenerative properties of zinc oxide (ZnO) and hydroxypropyl cellulose (HPC) was produced. Two types of dressings were successfully printed by varying the concentrations of ZnO and HPC: ZnO:HPC at 11:10 and 20:20 % (w/v). Both inks presented an adequate rheological shear-thinning behavior, resulting in wound dressings with a stable matrix structure. Moreover, to grant antimicrobial and antibiofilm activity, an octenidine (OCT)-hydrogel was loaded into the dressing's macropores. The unloaded dressings with ZnO at 20 % (w/v) and all the OCT-loaded dressings presented antibiofilm activity, showing a biofilm reduction of ~ 75 % against *S. aureus*. *In vitro* cellular assays indicated that the unloaded dressings provided regenerative potential by showing wound closure approximately completed in 48 h, highlighting the regenerative potential of the Alg:ZnO:HPC ink. These dressings exhibited *in vitro* and *in vivo* cytocompatibility, along with regenerative potential evidenced by collagen deposition and rapid wound closure. OCT-loaded matrices retained the regenerative potential and biocompatibility of the unloaded dressings, supporting their suitability as a platform for advanced wound management.

1. Introduction

Each year, millions of patients worldwide are adversely affected by chronic, non-healing wounds (Falanga et al., 2022). While numerous treatments are currently available on the market, and increasingly effective therapies emerge each year, chronic wounds continue to represent an urgent social, psychological, and economic burden due to the complexity of their diagnosis and treatment (Falanga et al., 2022; Las Heras et al., 2020; Shukla et al., 2026). The concept of the ideal dressing can be described as the one that combines features that will directly promote and stimulate the healing process but also regulate critical wound conditions (i.e., exudate, moisture, infection, pain, odor), leading to the healing progression in a timely and efficient way for a given patient (Zhou et al., 2024; Fan et al., 2022; Zöller et al., 2025).

* Corresponding author at: Research Institute for Medicines (iMed.ULisboa), Faculty of Pharmacy, Universidade de Lisboa, Avenida Prof. Gama Pinto, 1649-003 Lisboa, Portugal.
E-mail address: iribeiro@ff.ulisboa.pt (I.A.C. Ribeiro).

https://doi.org/10.1016/j.ijpharm.2026.127356
Received 5 July 2026; Received in revised form 25 August 2026; Accepted 27 August 2026
Available online 1 September 2026

However, due to the heterogeneity of the wound, the features that need to be employed will differ from patient to patient. To achieve innovative, customized wound dressings, a suitable technology equipped with appropriate tools is required to rapidly adapt to the dressing geometry and patient-specific needs (Fan et al., 2022). To tackle this, 3D printing technology can be used to develop novel treatments for wound patients and improve their outcomes. 3D printing has been highlighted as a major tool in the medical community to produce personalized treatments tailored to the patient's needs and characteristics that can be quickly changed (Las Heras et al., 2020). Several 3D printing strategies can be employed, including the fabrication of wound dressings using polymeric hydrogels as printable inks, combined with active materials that promote and improve wound healing (Chen et al., 2025; Kim et al., 2026; Lin et al., 2026; Teoh et al., 2022). A suitable polymer for formulation of inks is alginate, a natural polysaccharide found in seaweed (particularly brown algae) and certain microorganisms (Umoren et al., 2022; Paques et al., 2014; Mallakpour et al., 2021). It is well known for its biocompatibility (Mallakpour et al., 2021; Sharma et al., 2024), non-toxicity (Paques et al., 2014; Mallakpour et al., 2021; Sharma et al., 2024), affordability (Paques et al., 2014; Mallakpour et al., 2021), and easiness to produce hydrogels (Paques et al., 2014). These hydrogels also present the ability to incorporate active agents (Mazurek et al., 2025; Rahaman et al., 2024), absorb exudates (Sharma et al., 2024; Mazurek et al., 2025) and show hemostatic activity (Sharma et al., 2024; Barsky et al., 2022), which are decisive features to build an ideal dressing. To improve the active properties of an alginate-based hydrogel ink, zinc oxide (ZnO) can be added to the ink for its biocompatible (Su et al., 2019), regenerative (Su et al., 2019; Yang et al., 2022) and antimicrobial activity (Su et al., 2019; Yang et al., 2022), aiming to solve several critical issues of the healing process through a single wound dressing. Nevertheless, since pristine alginate-based hydrogels tend to present a lack of printability, resolution and shape fidelity (Mallakpour et al., 2021; Fang et al., 2023), the use of a viscosity-modulating agent (e.g., cellulose (Vajda et al., 2025); gums (Torres-Ayala et al., 2025); starch (Cardoso et al., 2025); gelatin (Ahmadi Soufivand et al., 2023) may be needed to improve rheological properties of the ink (Yalman et al., 2025; Silva et al., 2025).

This study aimed to develop a 3D-printed innovative wound dressing platform that combines regenerative properties with on-demand antimicrobial functionality. To this end, a novel semi-solid extrusion ink composed of alginate, zinc oxide, and hydroxypropyl cellulose was produced. A key innovation of this platform lies in its modular post-printing functionalization strategy, whereby the interconnected pores of the 3D-printed matrix can be loaded with an octenidine dihydrochloride (OCT)-based hydrogel after fabrication. This approach enables the same dressing architecture to be adapted according to the clinical needs of the wound, generating two therapeutically distinct versions from a common wound dressing: an unloaded dressing that provides a regenerative microenvironment to support tissue repair in non-infected wounds, and an antimicrobial dressing capable of delivering OCT (model-drug) to prevent microbial colonization and biofilm formation in infected wounds. By combining regenerative and antimicrobial functionalities within a single manufacturing platform, this versatile design represents a customizable strategy for the management of wounds at different stages of the healing process. The cytocompatibility and the regenerative potential of the developed dressings were evaluated using both *in vitro* and *in vivo* models.

2. Materials and methods

2.1. Materials

Alginic acid sodium salt from brown algae (with a mannuronic acid and guluronic acid ratio of ≈1.56; MW: 240 kDa), from Sigma Aldrich (Steinheim, Germany); low-substituted Hydroxypropyl Cellulose (MW: 33 kDa, 5.0–16.0 % of hydroxypropyl groups) and citric acid monohydrate from Glentham Life Science (Corsham, United Kingdom); Zinc oxide and 1,1′-(Decane-1,10-diyl)bis(N-octylpyridin-4(1H)-imine) dihydrochloride from BLDpharm (Hamburg, Germany); Trisodium citrate, Potassium dihydrogen phosphate and Tween®80 (Polysorbate) from Merck (Darmstadt, Germany); Calcium Chloride from PanReac AppliChem (Barcelona, Spain); and water purified by Sartorius purification system (Arium® pro).

2.2. Production of a 3D-printed regenerative dressing

2.2.1. Preparation of the dressing's ink formulation

To produce the most suitable ink for the dressing matrix, different formulations were prepared combining alginate (Alg) with Zinc Oxide (ZnO) as main constituents.

Firstly, alginate hydrogels were prepared by dissolving Alg in purified water to produce an Alg aqueous solution at 3, 4, 5 and 6 % (w/v). The solution was stirred for 30 min at 800 rpm in a heated bath at 65°C (VELP Arex-6 Digital Pro, Usmate Velate, Italy). At the end, an alginate hydrogel was obtained.

The Alg:ZnO hydrogels were prepared by weighing the required amount of ZnO and dispersing it directly into the alginate hydrogel under continuous stirring until a homogeneous formulation was obtained. Final ZnO concentrations of 11 and 20 % (w/v) produced Alg:ZnO hydrogels with alginate-to-ZnO ratios of 5:11 and 5:20, respectively.

To improve the printability of the Alg-ZnO formulations, hydroxypropyl cellulose (HPC) was added at varying concentrations. Firstly, purified water was added to Alg to produce an Alg aqueous solution at 10 % (w/v). The solution was stirred for 30 min at 800 rpm in a heated bath at 65°C. After cooling the alginate solution, different amounts of ZnO were added, and the resulting mixtures were subsequently combined with HPC to produce inks containing final ZnO concentrations of 11 % or 20 % (w/v) (Alg:ZnO). Simultaneously, an HPC mixture was prepared according to previously performed work of Gan et al. (2021) by combining the HPC with purified water to achieve the final concentrations of 2.5, 5, 10 and 20 % (w/v). A final alginate concentration of 5 % (w/v) was obtained through nominal dilution. The HPC solution was first stirred at 800 rpm for 30 min at room temperature, followed by stirring at 800 rpm for 1 h at 70°C. The hot HPC solution was poured into the Alg:ZnO (previously heated until reaching 70°C) and stirred for 1 h at 800 rpm at 90°C. Following formulation, the resulting Alg:ZnO:HPC systems exhibited the following composition ratios (w/v): 5:11:2.5, 5:11:5, 5:11:10, 5:11:20, 5:20:2.5, 5:20:5, 5:20:10, and 5:20:20. All mixtures were kept at 4°C until further use.

2.2.2. Parameters of the 3D printing process

All produced formulations were inserted into the extrusion polypropylene syringes with 5 cm^3 of volume coupled to dispensing tips with a 0.58 mm nozzle (QuantX™ Precision, Dispense tips). An extrusion 3D printer, Regemat 3D bioprinter (Regemat 3D BIO V1, Granada, Spain) combined with the Regemat design software (Regemat 3D designer, Granada, Spain) was used to print porous cube-shaped dressings, 1 x 19.6 x 19.6 mm (height x width x length), with square pores with a size of 2 x 2 mm at room temperature. Predefined software conditions were chosen as the optimal settings, including: a layer height of 0.41 mm, a diagonal infill pattern with a 90° angle and a flow speed of 2 mm/s. Then, the software assigned the number of layers (three layers) based on these parameters. The full dressing printing parameters are presented in Fig. 1.

2.2.3. Optimization and evaluation of the 3D printing performance

The printing performance was evaluated by assessing the overall appearance of the printed scaffolds through photographs taken after each printing process and comparing them with the corresponding 3D model design (Fig. 1). Printability was characterized by evaluating qualitative attributes such as the matrix layout, pore conformation and

Printing parameters	Speed (mm/s)
Retract speed	5
Perimeter speed	10
Infill speed	5
Travel speed	30

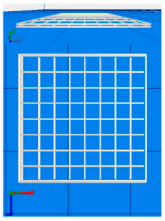

Fig. 1. Speed parameters used for printing the 3D wound dressings and corresponding CAD model. Speed parameters: flow speed during retract/compensation actions (Retract speed) and printhead movement speeds during printing, including perimeter speed, infill speed, and travel speed.

overall appearance when comparing with the theoretical 3D model. In addition, quantitative attributes were evaluated, such as the total number of printed pores (NTP), since, according to the used geometrical configuration, the maximum possible number of pores was 64. The total number of pores in percentage was calculated according to equation (1):

$$NTP(\%) = \frac{P_n}{64} \times 100 \quad (1)$$

where P_n is the total number of pores achieved per printed dressing.

The printability as a quantitative attribute to evaluate square-shaped pores was calculated according to equation (2) (Ouyang et al., 2016):

$$Pr = \frac{L^2}{16A} \quad (2)$$

Where L represents the perimeter of the pore in mm and A the area of the pore in mm^2. According to equation (2), an ideal P_r value is 1, representing excellent gelation, which means that the pores of the 3D dressing were properly printed, and the matrix strands and layers did not fuse (Ouyang et al., 2016).

A relation between the Printability and the total number of printed pores, namely Quality of the Scaffold ($Q_{scaffold}$), was calculated using equations (3) and (4) (Cardoso et al., 2023):

$$Q_{scaffold} = \frac{P_r \times P_n}{P_{max}}, \ if\ P_r \leq 1 \quad (3)$$

$$Q_{scaffold} = \frac{1 - (1 - P_r) \times P_n}{P_{max}}, \ if\ P_r > 1 \quad (4)$$

where P_r represents the printability of the dressing, P_n the total number of pores in the printed dressing and P_{max} the maximum number of pores achievable per printing process. A $Q_{scaffold}$ value of 1 indicates an excellent printed dressing, with all theoretical pores successfully reproduced and exhibiting excellent resolution, gelation, and printability.

2.3. 3D-printed dressings with regenerative and antimicrobial properties

2.3.1. Preparation of the dressing's matrix

Two types of dressings were prepared: WD_{11}, containing 5 % (w/v) alginate (Alg), 11 % (w/v) ZnO, and 10 % (w/v) hydroxypropyl cellulose (HPC); and WD_{20}, containing 5 % (w/v) alginate, 20 % (w/v) ZnO, and 20 % (w/v) HPC.

The dressings were prepared according to section 2.2.1. After printing, the dressings were immersed in a 4 % (w/v) $CaCl_2$ solution for 10 min.

2.3.2. Preparation of a drug-loaded hydrogel

A drug-loaded hydrogel with antimicrobial activity was prepared by incorporating octenidine dihydrochloride (OCT) with a final concentration of 0.1 % (w/v) in an alginate hydrogel at 5 % (w/v) prepared with citrate buffer (0.1 M) at pH 6. OCT was accurately weighed, and ethanol was added, followed by vortexing until complete drug dissolution. Then, citrate buffer was added to this ethanolic solution and vortexed for homogenization. The final ethanol concentration in the formulation was 10 % (v/v). Afterwards, the prepared OCT solution was slowly added to the Alg powder under continuous stirring until complete homogenization was achieved. The resulting formulation was designated as Ink_{OCT}. For comparison purposes, a drug-free hydrogel consisting of 5 % (w/v) Alg was prepared under identical conditions and designated as Ink_{Alg}. All mixtures were kept at 4°C until further use.

2.3.3. Optimization of the infill printing process

The Ink_{OCT} was placed into an extrusion metallic syringe with 3 cm^3 of volume coupled to a stainless-steel dispense tip with a 0.65 mm (19G) of nozzle tip. To optimize the hydrogel filling, the following parameters were tested: amount of filling from 10 to 200 (μL/layer) and compensate 1 to 4 (μL). The other infill parameters were kept constant: offset "Z" 0 mm, retract 0 mm/s, retract speed 1 mm/s and purge 0 mm. After printing, the loaded dressings were immersed in a $CaCl_2$ solution at 4 % (w/v) for 10 min.

2.3.4. Inks rheological characterization

Rheological characterization of the produced formulations was performed using a Malvern Gemini HRnano rotational rheometer (Malvern Panalytical, United Kingdom). The rheometer was equipped with a Peltier plate temperature control system (± 0.01°C) and a parallel-plate geometry with a 20 mm diameter and a 1.0 mm gap.

Steady-shear flow measurements were initially conducted to characterize the viscosity behavior of all Alg:ZnO:HPC formulations at 25°C over a shear rate range of 0.05–10 s^{-1}.

Following the selection of the most suitable inks for further investigation, steady-shear flow measurements were performed in triplicate for the dressing matrix inks (Ink_{11} and Ink_{20}) and the filler inks (Ink_{OCT} and Ink_{Alg}) under the same experimental conditions (0.05–50 s^{-1} and 25°C).

Oscillatory shear measurements were subsequently carried out to evaluate the storage modulus (G′) and loss modulus (G″) within the linear viscoelastic region (LVR), ensuring that the measured moduli were independent of strain. The LVR was determined by amplitude sweep tests performed at an angular frequency of 6.28 rad·s^{-1} (1 Hz), over a strain range of 0.01–100 %. Frequency sweep measurements were then conducted within the LVR at a constant strain of 1 %, over a frequency range of 0.1–100 Hz. All measurements were performed at both 25 and 37°C for the matrix and drug-loaded inks. Rheological data were analyzed using GraphPad Prism 11 (version 11.1.0; GraphPad Software, San Diego, CA, USA).

2.4. Characterization of printed dressings

For the dressing's characterization, all printed dressings were cut into four square pieces (≈9.8 x 9.8 mm).

2.4.1. Physicochemical characterization

Scanning Electron Microscopy (SEM) was performed to evaluate the matrix and the macropore structure of each printed dressing. Firstly, each dressing was freeze-dried for 24 h (Christ Alpha 1–4, B. Braun Biotech International, Melsungen, Germany). Afterward, the samples were placed on an Al stub using double-sided carbon tape and sputter-coated with a thin Au/Pd film in a Quorum Technologies coater, model Q150T ES. For the morphology analysis, they were then analyzed in a Hitachi scanning electron microscope (SEM), model S2400, with digital image acquisition by Bruker, software Quantax Esprit 1.9. For the topography and roughness analysis, the samples were analyzed in a ThermoScientific desktop SEM, model Phenom ProX G6, with a CeB6 filament and with digital image acquisition using the Phenom User Interface.

To identify the different functional groups of wound dressing components, Attenuated Total Reflection Fourier-Transform Infrared (FTIR-

ATR) spectroscopy was performed using the Nicolet™ iS™5 FTIR Spectrometer (Thermo Fisher Scientific, Massachusetts, USA) coupled with iD5 ATR (Thermo Fisher Scientific, Massachusetts, USA). The infrared spectrum was obtained with a total of 16 scans and a resolution of 4 cm^{-1}, with absorbance readings from 4000 to 600 cm^{-1}.

2.4.2. Antimicrobial activity

2.4.2.1. Microorganisms. *S. aureus* ATCC 25923 obtained from the American Type Culture Collection (ATCC) was selected for these experiments. Cultures were obtained from *S. aureus* frozen stocks (−80°C), plated on tryptic soy agar (TSA) prepared by supplementing tryptic soy broth (TSB, Biokar Diagnostics) with Bacteriological Agar Type E (Biokar Diagnostics), and incubated at 37°C for 24 h (VWR®, INCU-Line® 150R, Pennsylvania, USA).

2.4.2.2. Free-octenidine and free-ZnO antimicrobial activity. The antimicrobial susceptibility of *S. aureus* to OCT and ZnO was assessed using the broth microdilution method, as previously described (Narciso et al., 2023). Briefly, two-fold serial dilutions of the active compounds were prepared in cation-adjusted Mueller-Hinton Broth (MHB; Biokar Diagnostics). Final concentrations ranged from 0.12 to 64 μg mL^{-1} for OCT and from 0.12 to 64 mg mL^{-1} for ZnO. Bacterial inocula were prepared in MHB to achieve a final concentration of approximately 5 × 105 CFU mL^{-1} in each well.

For OCT, the minimum inhibitory concentration (MIC) was determined after 24 h of incubation at 37°C by measuring absorbance at 595 nm using a microplate multimode detector (Anthos Zenyth 3100). Due to the interference of ZnO with optical density measurements, the MIC of ZnO was determined using a resazurin-based viability assay, following the methodology described by Pontes et al. (2016). The MIC, defined as the lowest concentration at which no bacterial growth or metabolic activity was detected. Positive controls consisted of inoculated growth medium, whereas negative controls included non-inoculated medium and non-inoculated ZnO-containing medium at each tested concentration.

For determination of the minimum bactericidal concentration (MBC), aliquots from wells with no visible growth from the MIC assay were transferred to a fresh 96-well microplate containing culture medium and incubated at 37°C for 24 h. Subsequently, bacterial growth was evaluated by measuring absorbance at 595 nm. The MBC was defined as the lowest concentration resulting in the absence of detectable bacterial growth.

2.4.2.3. Inhibition of bacterial growth. To test if the 3D-printed dressings (unloaded and loaded with OCT) were able to inhibit *S. aureus* growth, the Kirby-Bauer test was conducted according to an adapted protocol (Severo et al., 2021; Vieira et al., 2024). Fresh *S. aureus* colonies grown on tryptic soy agar (TSA) plates were suspended in Mueller-Hinton broth and adjusted to a turbidity equivalent to 0.5 McFarland units (approximately 1.5–2 × 10^8 CFU/mL) using a cell density meter (Ultrospec 10, Biochrom). A sterile cotton swab was immersed in the standardized bacterial suspension, and excess liquid was removed by pressing the swab against the inner wall of the tube. Mueller–Hinton agar (MHA) plates, prepared using Mueller–Hinton broth (MH, Biokar Diagnostics) supplemented with Bacteriological Agar Type E (Biokar Diagnostics), were uniformly inoculated by swabbing the entire agar surface (CLSI Performance Standards for Antimicrobial Disk Susceptibility Tests, 2024). An octenidine (OCT) disk (30 μg) was included as a positive control. Subsequently, one sample of each 3D dressing (WD_{11}, ALG-WD_{11}, OCT-WD_{11}, WD_{20}, ALG-WD_{20}, and OCT-WD_{20}) was placed on the surface of the inoculated MH agar plates. The plates were incubated at 37°C for 24 h. Antimicrobial inhibition was evaluated by measuring the inhibition halos using a digital Vernier caliper (Powerfix® Profi+, Neckarsulm, Germany). The assay was performed in triplicate.

2.4.2.4. Antibiofilm activity. The antibiofilm activity of the printed dressings was assessed against *S. aureus* using piglet skin as a skin model. The fat layer was first removed from the piglet skin, and the skin was cut into square pieces (1 x 1 cm). The obtained samples were aseptically handled, washed with sterile purified water, and subsequently immersed in 70 % (v/v) ethanol for 15 min. Finally, the skin pieces were exposed to UV light for 15 min and fixed to the bottom of 24-well culture plates using liquid silicone, as previously described (Mendes et al., 2021). One sample of each 3D dressing (WD_{11}, ALG-WD_{11}, OCT-WD_{11}, WD_{20}, ALG-WD_{20}, and OCT-WD_{20}) was then placed on the surface of each skin piece. Subsequently, Brain Heart Infusion (BHI) medium (Biokar Diagnostics) supplemented with 1 % (w/v) glucose (Glu) was added to each well. A bacterial suspension was prepared from a fresh *S. aureus* TSA 24 h-culture plate, by adjusting to 1 McFarland unit in BHI-Glu 1 % (w/v) medium. Suitable dilutions were performed to achieve a final concentration of 3.0 × 10^6 CFU/mL in each inoculated well. For each tested dressing (unloaded and loaded with Ink_{Alg} or Ink_{OCT}), inoculum-free BHI + Glu medium was used as the negative control. In addition, inoculated wells containing piglet skin but no dressing samples were used as the positive control. The 24- well culture plates were incubated at 37°C for 24 h. After incubation, the culture medium and the printed dressing were removed from each well. The wells containing the piglet skin samples were then washed twice with 1 mL of sterile water. The skin was removed and placed in 1 mL of NaCl at 0.9 % (w/v). To detach the sessile bacteria, the samples were sonicated (P Selecta® Ultrasons, J.P. Selecta, Barcelona, Spain) and vortexed (RSLAB-6PRO) for 4 min. Suitable dilutions were performed and 20 μL of each diluted sample was spread on top of Mannitol salt (MA, Biokar Diagnostics) agar plates. The MA agar plates were incubated at 37°C for 24 h. Finally, the biofilm was evaluated by counting the Colony Forming Units (CFU) in each plate. The assay was performed in quadruplicate for each tested dressing, including the skin without the dressing (control), in two independent assays.

For statistical analysis, the Shapiro–Wilk test was used to confirm the normal (Gaussian) distribution of the data, followed by the Student's *t*-test as a parametric test.

2.4.3. In vitro release of OCT

To quantify the amount of drug released from the dressings over time, an *in vitro* release study was conducted using vertical Franz diffusion cells with an effective diffusion area of 1 cm^2 (Nobre et al., 2025). A circular synthetic polyethersulfone (PES) membrane (Supor™, 0.45 μm pore size, 1 cm^2 diameter, Pall Corporation, New York, USA) was mounted between the donor and receptor compartments. The receptor compartment was filled with 4 mL of phosphate buffer (0.05 M, pH 5.6) containing Tween® 80 (0.1 %, w/v) as a surfactant. A pH of 5.6 was selected to mimic the slightly acidic physiological pH of the skin, reflecting the intended application of the dressings.

Dressings (~9.8 × 9.8 mm) were placed in the donor compartment on top of the PES membrane. ALG-WD_{11} and ALG-WD_{20} dressings were tested as blank controls, whereas OCT-WD_{11} and OCT-WD_{20} dressings were evaluated for octenidine release. The experiments were conducted under continuous stirring at 250 rpm and maintained at 32 ± 1°C (VELP, stirring plate, Italy, and VWR® INCU-Line® IL 150R, Belgium), corresponding to the average skin surface temperature.

The release assay was carried out for 72 h. At predetermined time intervals, 200 μL aliquots were withdrawn from the receptor medium and immediately replaced with an equal volume of fresh phosphate buffer containing Tween® 80 (at 32 ± 1°C) to maintain sink conditions and a constant receptor volume throughout the experiment.

The collected samples were transferred to a 96-well microtiter plate and analyzed using UV–Vis spectrophotometry (SPECTROstar® Omega, BMGLabtech, Germany) at 281 nm. An OCT calibration curve (ranging from 1 to 32 μg/mL) was prepared from an OCT aqueous stock solution (0.1 % w/v). Octenidine incorporated into the alginate hydrogel was also determined using the same quantification method.

2.4.4. In vitro cytocompatibility and evaluation of regenerative potential

The cytocompatibility and regenerative potential of ZnO-alginate-based printed dressings were evaluated in human dermal fibroblast cultures (AG22719, Coriell Institute for Medical Research). Cells were maintained in α-Minimal Essential Medium (α-MEM) supplemented with 10 % fetal bovine serum (FBS), 100 IU/mL penicillin, 100 μg/mL streptomycin, and 2.5 μg/mL amphotericin B (all from Gibco). Cultures were incubated at 37°C in a humidified atmosphere of 5 % CO_2. When cultures reached approximately 70 % confluence, cells were detached and reseeded in 24-well culture plates at a density of 1 x 10^4 cells/cm^2 in the same defined medium. After 24 h, permeable inserts with 0.4 μm pores (Thincert, Greiner) containing the test materials were placed into the wells with the cultured cells, using a total culture-medium volume of 1.0 mL per well. This configuration enabled the diffusion of leachables from the materials to the cell cultures. Cells maintained under identical experimental conditions with empty ThinCert inserts served as the negative control (C−).

2.4.4.1. Metabolic activity. The metabolic activity of the human dermal fibroblast (HDF) cultures was evaluated using the resazurin assay. After 24 h of leachate exposure, the culture medium was replaced with fresh medium supplemented with 10 % (v/v) resazurin sodium salt (Sigma-Aldrich) and incubated for 3 h at 37°C. Following incubation, the supernatant fluorescence was measured using a microplate reader (Synergy HT, BioTek, USA) with the following settings: excitation, 530 nm; emission, 590 nm. All measurements were performed in triplicate.

2.4.4.2. Cytotoxicity. The cytotoxicity potential of the developed materials was assessed by quantifying lactate dehydrogenase (LDH) released in the culture medium. Following 24 h, supernatants were collected and incubated with the LDH-constituted solution (TOX-7 kit, Sigma-Aldrich) for 30 min at room temperature. The reaction was stopped by adding 1 M HCl. Absorbance was measured at a primary wavelength of 490 nm, with background correction at 690 nm. The assay was performed in triplicate.

2.4.4.3. Collagen staining. Collagen staining was performed after 24 h of incubation. Subsequently, HDF cultures were fixed with 1.5 % glutaraldehyde for 10 min and washed with phosphate-buffered saline (PBS). Cultures were stained with 0.1 % (w/v) Sirius Red–picric acid solution and incubated for 1 h at room temperature, protected from light. After staining, the cultures were rinsed with 0.01 M HCl to remove excess dye. Images were acquired using a Zeiss Axiolab 5 microscope equipped with an Axiocam 5 Color camera. The collagen-stained area was quantified in ImageJ (v.1.54 g, National Institutes of Health, Bethesda, MD, USA) using the Huang thresholding algorithm. The assay was performed in triplicate.

2.4.4.4. Wound-healing potential. The wound-healing potential of the developed materials was evaluated using the scratch assay. Cells were cultured without the materials until reaching approximately 70 % confluence. The monolayer was then scratched using a 10-μL micropipette tip, and images were immediately acquired (time point 0 h) using an inverted microscope equipped with an Axiocam 5 Color camera (Zeiss Axiolab 5, Carl Zeiss AG, Aalen, Germany). ThinCert inserts containing the tested materials were subsequently positioned above the scratched monolayers, allowing indirect exposure to released components without direct contact between the dressings and the cells. Cultures maintained with empty ThinCert inserts served as the negative control (C −). Cultures were incubated under these conditions for 48 h, and additional images were captured at 24 h and at the end of the assay. Wound closure was quantified using ImageJ software by analyzing a predefined area of each image and applying the following expression:

$$Woundhealing(\%) = (Ai - AF/Ai)x100\% \quad (5)$$

where A_i and A_F represent the scratched areas before and after the incubation with the developed materials. Measurements were performed in triplicate.

Statistical analysis was conducted using the GraphPad Prism 10. Ordinary one-way analysis of variance (ANOVA) followed by Tukey's multiple comparisons test was performed. Significance was set at $p \leq 0.05$. Results were presented as mean ± standard deviation (SD).

2.4.5. In vivo evaluation

All the procedures were performed in agreement with the European Council Directive (2010/63/EU) and approved by the local Committee Responsible for animal welfare (ORBEA) of UTAD (project number 232-e-USBB-2024) and the General Directorate of Food and Veterinary Medicine (reference number 36606/25-S). A total of 12 Male Wistar rats, 10 weeks old and weighing 270–300 g, sourced from a certified vendor (IBMC, Porto, Portugal), were used for the subcutaneous implantation model. The required sample size was calculated a priori using G*Power (v. 3.1.9.6, Düsseldorf, Germany), based on a randomized complete block design, assuming $\alpha = 0.05$, $1\text{-}\beta = 0.8$, and an effect size of 0.5.

Animals were randomly assigned to groups of four and housed under controlled temperature and humidity conditions, and a 12:12 h light–dark cycle, with ad libitum access to food and water. After a seven-day acclimatization period, animals were anesthetized via intraperitoneal injection of ketamine 90 mg/Kg (Ketamidor®, Richter Pharma) and xylazine hydrochloride 10 mg/Kg (Seton®, Calier). Following confirmation of anesthetic depth, the dorsal region of each animal was trichotomized and aseptically prepared using a chlorhexidine-based solution. Before implantation, the dressings were surface-decontaminated by UV-C irradiation for 30 min on each side inside a biosafety cabinet. The samples were then transferred using sterile forceps to sterile, closed containers and maintained under aseptic conditions until implantation. During surgery, the dressings were handled exclusively with sterile instruments. After skin incisions, six subcutaneous pockets were gently created using blunt dissection, and tested samples (1 cm^2) were randomly distributed through the subcutaneous pockets. The incision was then closed with interrupted monofilament sutures (4/0 Dafilon, B Braun). Postoperative analgesia consisted of buprenorphine (Bupaq® Richter Pharma) at a dose of 0.03 mg/kg, administered over 24 h. Enrofloxacin (Baytril®, Elanco) was administered subcutaneously at a dose of 10 mg/kg once daily for three consecutive days postoperatively. Animals were monitored daily for signs of distress or complications.

At predetermined time points (7 and 15 days), animals were euthanized using an intraperitoneal injection of pentobarbital sodium (Euthanimal 40 %®, NePhar) at a dose of 150 mg/kg, followed by a systematic necropsy. Implant sites, including surrounding tissue, were carefully excised and fixed in 4 % buffered formaldehyde. Then, samples were embedded in paraffin and cut longitudinally into 5 μm-thick sections. Sections were stained with hematoxylin and eosin (H&E) and examined under a light microscope (Axiolab 5 microscope coupled with Axiocam 5 Color Camera, Zeiss, Oberkochen, Germany). Local tissue response was evaluated semi-quantitatively in accordance with the ISO 10993–6 guidelines. The inflammatory infiltrate, comprising polymorphonuclear cells, lymphocytes, plasma cells, macrophages, and giant cells, was scored alongside reactive tissue changes, including necrosis, neovascularization, fibrosis, and fatty infiltration. Each parameter was graded on a 5-point severity scale: 0 (absent), 1 (minimal), 2 (mild), 3 (moderate), and 4 (severe/extensive). Dressings were categorized based on their total irritancy score as non-irritant (≤ 2.9), slight (3.0–8.9), moderate (9.0–15.0), or severe irritants (> 15.0). The assay was performed in sextuplicate.

3. Results and discussion

3.1. Regenerative dressing matrix development

Following the selection of the two main ink constituents (Alg and ZnO), the first step was to determine the suitable amount of each material to produce the hydrogel. A preliminary study evaluated different alginate concentrations while keeping printing conditions constant (Table SM_1). All inks could be extruded without nozzle clogging, but printability remained low, with fewer than 45 % of the expected 64 pores produced. Formulations containing 5 % and 6 % (w/v) alginate showed the highest pore numbers and the most uniform structures. Since formulations containing 5 % and 6 % (w/v) alginate showed similar performance, 5 % (w/v) was selected for further studies, and inks incorporating 11 % and 20 % (w/v) ZnO were subsequently prepared.

Besides expecting to provide antimicrobial and regenerative benefits (Yang et al., 2022), ZnO improved printability and structural stability, increasing pore formation to nearly 30 pores. Therefore, both formulations were retained for further studies. However, the printed structures still showed poor uniformity, low resolution, and collapsed macropores, consistent with the limited mechanical strength commonly reported for alginate-based inks, which negatively affects printability and reproducibility (Murab et al., 2022; Kong et al., 2025).

Thus, hydroxypropyl cellulose (HPC) was incorporated into the Alg:ZnO formulations at concentrations ranging from 0 to 20 % (w/v) to evaluate its effect on improving dressing printability. HPC was chosen to prevent dripping and pore coalescence during the printing process before crosslinking, while adding $CaCl_2$ as a crosslinking method provided structural fixation and dressings' stability.

The results of the HPC optimization are presented in Table 1 and Fig. 2. Overall, when comparing HPC-free formulations with the ones containing HPC at 5 % (w/v), an increase in the total number of printed pores per dressing was observed from 31 to 50 (ZnO formulations at 11 % (w/v)) and 31 to 45 (ZnO formulations at 20 % (w/v)). Increments of the HPC content in the samples with ZnO at 11 % (w/v) increased the total number of printed pores, better dressing resolution and uniformity, until 10 % (w/v) of HPC (59 pores) (Table 1). By increasing HPC to 20 % (w/v), no printed dressing was achieved since it was not possible to extrude the ink from the printing syringe. For the samples printed with ZnO at 20 % (w/v), increasing the HPC content led to an increase in the total number of printed pores, better dressing resolution and uniformity, with a maximum of 61 pores achieved when using 20 % (w/v) of HPC. Of all printed samples, the $S_{11:10}$ and $S_{20:20}$ presented the highest $Q_{scaffold}$ (0.86 and 0.90, respectively), close to the ideal value of 1. The addition of HPC proved to be critical for the printing process, as it significantly improved printability and enabled the fabrication of dressings that closely matched the theoretical 3D model (Fig. 1). It was possible to identify a trend regarding the improvement in the dressing's printability as a function of ZnO: HPC ratio added into the formulation (Fig. 2B). A 1:0 ratio proved to be inadequate, as the resulting $Q_{scaffold}$ value was lower than 0.43. A ratio of 2:1, showed an improvement in the dressing's resolution and appearance; however, the $Q_{scaffold}$ was still far from the ideal value of 1. The ratio of 1:1 presented the highest $Q_{scaffold}$, which translated to the best printed samples.

Table 1
Printability results with inks incorporating ZnO at 11 or 20 % (w/v) combined with different HPC percentages.

Sample name ($Ink_{ZnO\ \%:HPC\%}$)	ZnO % (w/v)	HPC % (w/v)	ZnO:HPC	NTP %	Pr	$Q_{scaffold}$	Power law index (n)
$Ink_{11:0}$	11	0	1:0	48 ± 21	1.41 ± 0.09	0.27 ± 0.11	0.911
$Ink_{11:2.5}$		2.5	4:1	45 ± 12	1.42 ± 0.10	0.25 ± 0.05	0.891
$Ink_{11:5}$		5	2:1	78 ± 9	0.93 ± 0.03	0.72 ± 0.07	0.812
$Ink_{11:10}$		10	1:1	93 ± 2	0.97 ± 0.05	0.86 ± 0.05	0.741
$Ink_{11:20}$		20	1:2	0	0	0	0.259
$Ink_{20:0}$	20	0	1:0	48 ± 12	1.18 ± 0.28	0.42 ± 0.20	0.890
$Ink_{20:2.5}$		2.5	8:1	54 ± 6	1.08 ± 0.02	0.50 ± 0.05	0.903
$Ink_{20:5}$		5	4:1	70 ± 1	1.38 ± 0.11	0.43 ± 0.07	0.864
$Ink_{20:10}$		10	2:1	68 ± 4	1.15 ± 0.19	0.55 ± 0.10	0.535
$Ink_{20:20}$		20	1:1	95 ± 1	1.06 ± 0.03	0.90 ± 0.02	0.550

To understand this trend and the impact of the addition of HPC into the formulation, the rheological profile of all inks was studied (Fig. 2C_1 and C_2). The results showed that the viscosity of all samples decreased with the increase of the shear rate, meaning the presence of shear-thinning behavior, the ideal rheological behavior for 3D inks aiming at an SSE-based process (Rau et al., 2023). Increasing the HPC content resulted in a more pronounced shear-thinning behavior (Fig. 2C_1 and C_2) and in the decrease of the power law index. The formulations that presented the highest $Q_{scaffold}$ showed a power law index of 0.741 and 0.550. These findings suggest that for the formulation of Alg:ZnO:HPC to be printed, a moderate shear-thinning behavior is needed. Finally, given the suitable results regarding the printability of the inks $S_{11:10}$ and $S_{20:20}$, both inks were selected to produce a regenerative matrix intended for wound dressings, and further designated as Ink_{11} and Ink_{20}, respectively. Following the selection of the ideal matrix ink, an optimization test was carried out to find out the critical printing parameters and their optimal values for the filling ink. The results regarding the infill process are presented on SM_2 (supplementary). From all infill parameters that were possible to change, the ones that were found to be critical to the process were the amount of ink per layer and the compensate parameter (Regemat 3D printer), where 200 μL and 4 mm/s were chosen, respectively.

3.2. Characterization of dressings

3.2.1. Morphology and chemical characterization

Regenerative dressings were produced using Ink_{11} and Ink_{20} to achieve WD_{11} and WD_{20} dressings, respectively (Fig. 3A). To evaluate the versatility of the dressing design, an octenidine-loaded hydrogel (Ink_{OCT}) was introduced into the pores of WD_{11} and WD_{20}, generating the customized constructs OCT-WD_{11} and OCT-WD_{20}, respectively. Loaded dressings with Ink_{Alg} were also produced as controls designated ALG-WD_{11} and ALG-WD_{20}.

The morphology of the printed dressings, including overall morphology, texture and topography, was analyzed by SEM (Fig. 3B, C, D). The results showed a difference in the shape of the macropores between 11 and 20 % (w/v) of ZnO. The dressings printed with Ink_{11} showed round-shaped macropores, while Ink_{20} showed a squarer shape. Assessing the 3D printing model used (Fig. 1), the format programmed for each macropore was square-shaped, so the dressings printed with Ink_{20} showed a higher shape fidelity compared to the model. Furthermore, when assessing the pore average for each ink used and comparing it with the CAD model (2x2 mm), a macropore average size around half of the digital 3D model was observed. These differences in the geometric configuration of the printed macropores could be related to the rheological properties of the used inks, leading to smaller-sized macropores

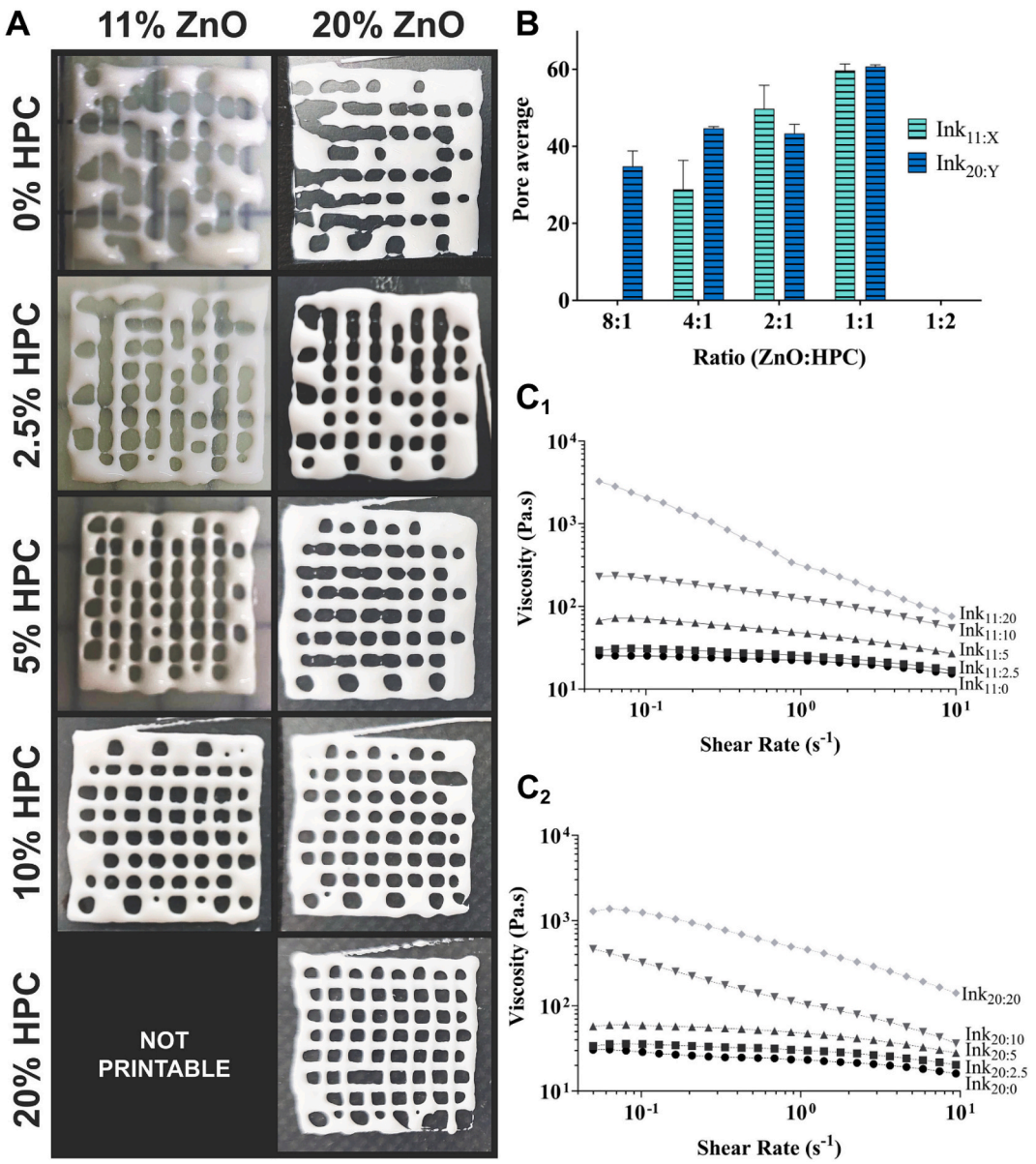

Fig. 2. A. Representative printed dressings obtained from the different ink formulations. B. Average number of macropores per dressing considering the different ratios of ZnO:HPC in the ink formulations. C. Flow curves showing the viscosity (Pa.s) as a function of shear rate (s^{-1}) for the inks with 11 % (w/v) of ZnO (C_1) and 20 % (w/v) of ZnO (C_2).

(Schwab et al., 2020).

Regarding the textural properties of the unloaded dressings, WD_{11} exhibited a more uniform matrix structure compared with WD_{20}.

The surface roughness profile presented in Fig. 3B was evaluated by measuring the Ra (average roughness) and Rz (average of maximum peaks and minimum valleys) in μm at six different points of the dressing (SM_3). Regarding the matrix of WD_{11} and WD_{20}, a lower Ra value was obtained in WD_{11} for all 6 analyzed zones, meaning that this dressing presented a smoother surface when compared to WD_{20}.

The produced dressings were characterized by FTIR-ATR spectroscopy (Fig. 3C). The resulting spectra exhibited the characteristic bands of the raw materials incorporated into the ink formulations, confirming their presence in the printed dressings. In the samples, the signal from the stretching vibrations of the O–H was observed at 3500–3200 cm^{-1}, as in alginate (3298 cm^{-1}) and HPC spectra (Vieira et al., 2024; Helmiyati and Aprilliza, 2017). Moreover, the corresponding peaks from alginate associated with the asymmetrical at 1595 cm^{-1} and symmetrical stretching vibrations at 1405 cm^{-1} of the $–COO^-$ band from the carboxylate anion (Vieira et al., 2024; Helmiyati and Aprilliza, 2017), the ether (–COC) of the glycosidic bond at 1081 and –CO stretching vibration at 1024 cm^{-1} (Vieira et al., 2024; Fang et al., 2025), were also observed in the dressing samples as in HPC (Alharbi and Guirguis, 2019; Halbus et al., 2025).

In the drug-loaded dressings, the band at 1599 cm^{-1} exhibited a more asymmetric profile than the corresponding band in raw alginate, which is associated with the asymmetric stretching vibrations of the $–COO^-$ group of the carboxylate anion. This change is attributed to the overlap between the alginate band at 1595 cm^{-1} and the C=N stretching vibrations of the octenidine ring band, observed around 1651 cm^{-1}. The resulting band broadening/asymmetry provides evidence of octenidine incorporation into the drug-loaded dressings (Helmiyati and Aprilliza, 2017; Černá et al., 2025; Pan et al., 2021).

Nevertheless, not all characteristic FTIR bands associated with octenidine could be identified in the drug-loaded dressings. This observation is likely related to the considerably lower concentration of octenidine (0.1 % w/v) compared with alginate (5 % w/v), resulting in

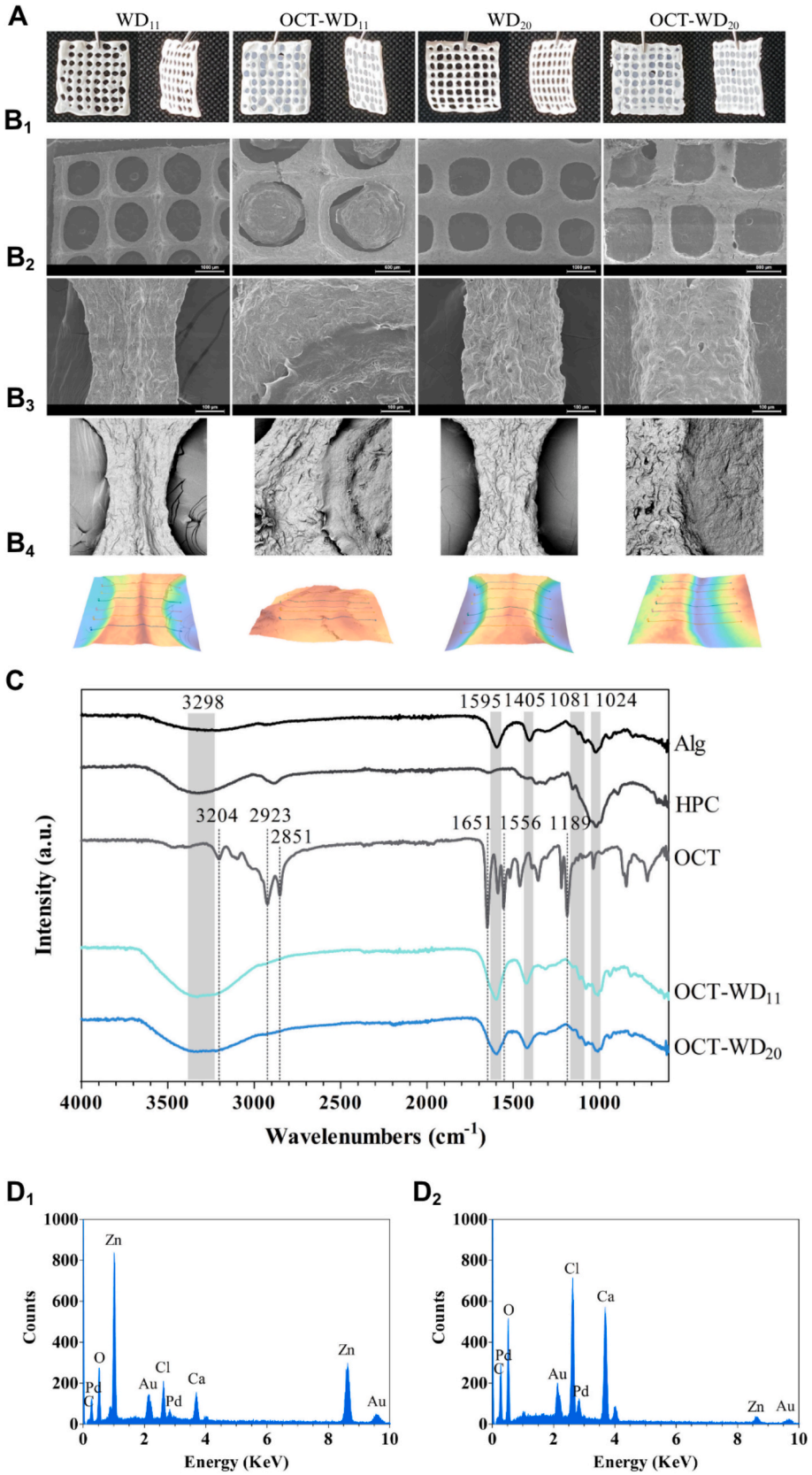

Fig. 3. Physicochemical characterization of the printed wound dressings. A. Photographs of unloaded and drug-loaded dressings. B. SEM imaging regarding a general overview of the matrix of the produced lyophilized dressings: macropores (B_1 and B_2), texture (B_3) and roughness profile (B_4). C. FTIR-ATR of the drug-loaded dressings and raw materials. D. Representative EDS analysis of the drug-free matrix (D_1) and drug-loaded pores (D_2).

reduced spectral intensity and potential overlap with the stronger absorption bands of the alginate. As a consequence, octenidine-specific vibrational features may not be readily distinguishable in the composite spectrum. This is likely the case for the bands at 3204 cm^{-1} (N–H stretching vibrations) and 1556 cm^{-1} (aromatic ring C=C stretching vibrations), which may be masked by overlapping alginate absorptions. Additional characteristic bands of octenidine could be expected at 2923 cm^{-1} and 2851 cm^{-1}, corresponding to the asymmetric and symmetric

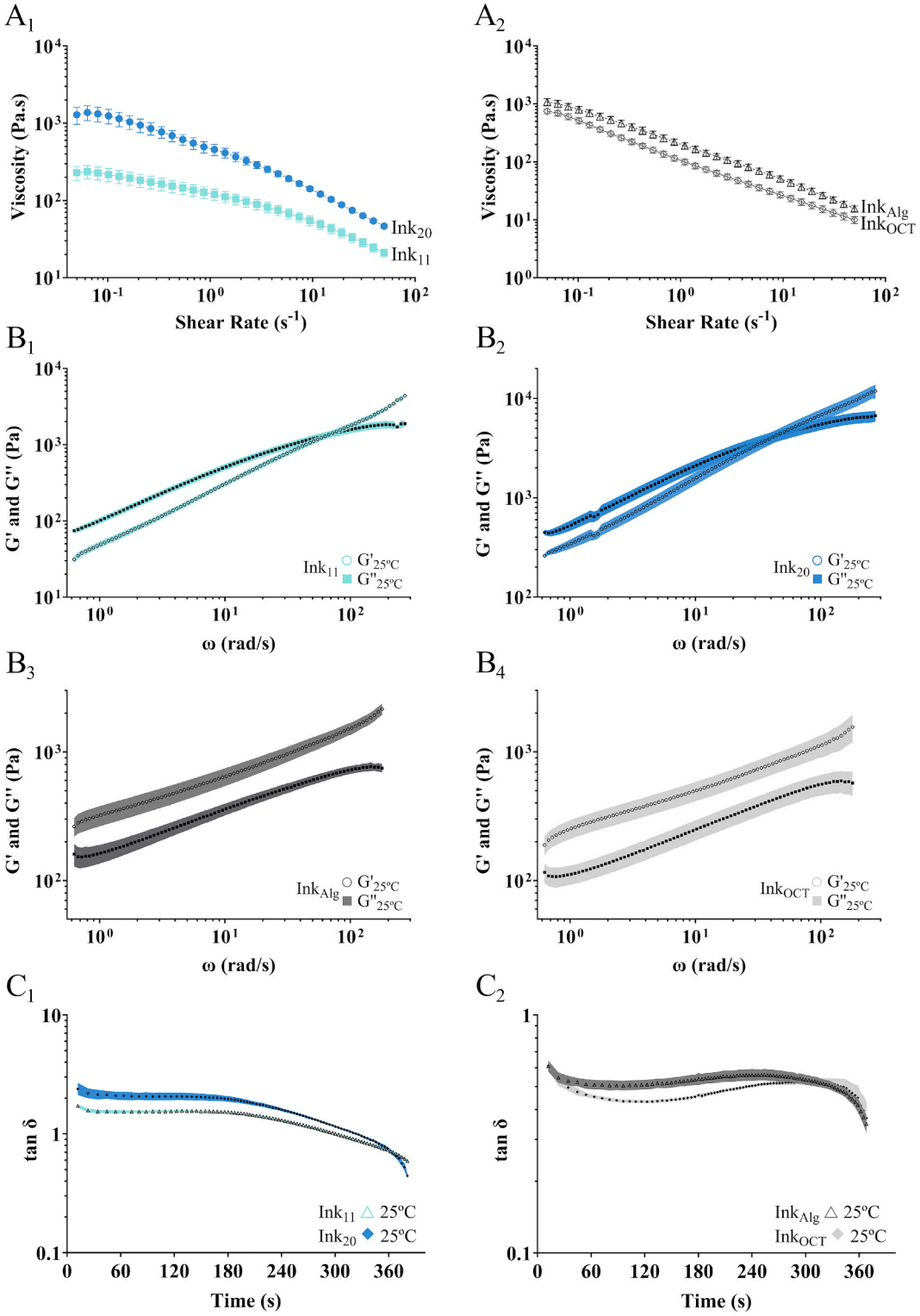

Fig. 4. Rheological evaluation of the matrix ($Ink_{11/20}$) and filling ($Ink_{Alg/OCT}$) inks at constant temperature (25°C). A. Flow curves regarding the viscosity (Pa.s) as a function of shear rate (s^{-1}), for $Ink_{11/20}$ (A_1) and $Ink_{Alg/OCT}$ (A_2). B. Oscillatory frequency sweep measurements showing the storage modulus (G' – represented by ○) and loss modulus (G'' – represented by ■) as a function of angular frequency (ω) for Ink_{11} (B_1), Ink_{20} (B_2), Ink_{Alg} (B_3), and Ink_{OCT} (B_4) at 25°C. C. The evolution of loss tangent (tan δ) as a function of time (s), for Ink_{11} (Δ) and Ink_{20} (◆) (C_1) and for Ink_{Alg} (Δ) and Ink_{OCT} (◆) (C_2). Data are presented as mean ± SD (n = 3). SD is represented by the colored lines.

C–H stretching vibrations, respectively, and at 1189 cm^{-1}, assigned to aromatic C–N stretching vibrations (Černá et al., 2025; Pan et al., 2021).

EDS analysis was used to evaluate the chemical composition of the drug-free dressing matrix and the drug-loaded dressing pores (Fig. 3D_1 and D_2). Regarding elemental composition, Zn was detected due to the addition of ZnO into the dressing matrix (Fig. 3D_1), while Ca and Cl were present in both samples (Fig. 3D_1 and D_2), corresponding to the main elements of the crosslinking system.

3.2.2. Rheology evaluation

The rheology of inks plays a crucial role in a 3D printing process, since it will determine if the ink presents suitable properties to be used (Rau et al., 2023). According to the results presented in Fig. 4A_1 and A_2, it was possible to verify that all gels used (filling and matrix gel) presented a shear-thinning behavior, since the viscosity (η) of the gel decreases with the increase of the shear rate. The presence of shear-thinning behavior is one of the major critical features of an ink intended for an extrusion-based process, since it avoids the formation of common 3D printing-related problems, such as the nozzle tip getting clogged, lack of uniformity, poor resolution, or even collapsed structures (Rau et al., 2023; Yuan et al., 2025). When the filling inks (Ink_{Alg} and Ink_{OCT}) were compared, Ink_{OCT} consistently exhibited lower viscosity (η) than Ink_{Alg} across all shear rates, indicating that the incorporation of OCT affected the rheological behavior of the formulation (Fig. 4A_2). Although Ink_{Alg}, was only produced for control purposes to compare the dressings loaded with the OCT, during the printing process it was possible to visualize, under the same printing conditions, that it was easier and more precise to extrude the drug-loaded gel into the dressings' macropores. Compared with Ink_{11}, Ink_{20} displayed substantially higher viscosity (η) across the entire range of shear rates. Notably, even the minimum viscosity of Ink_{20} exceeded all viscosity values measured for Ink_{11} (Fig. 4A_1). Regarding the printing process and the final structure of the printed dressings, samples printed with ZnO at 20 % (w/v) exhibited fewer interconnected macropores, reduced ink spreading within the matrix, and improved shape fidelity, with macropores that more closely matched the square geometry of the 3D model. This may suggest that printing with a higher viscosity (1287–142 Pa.s) led to better printing results of the Alg:ZnO:HPC mixture. In addition, based on the printing parameters used to print the 3D wound dressings (flow speed of 2 $mm{\cdot}s^{-1}$ and 0.58 mm of inner nozzle diameter), the viscosity values obtained as a function of shear rate are within an expected shear rate of 30 s^{-1} during the printing process. Nevertheless, not only is the presence of shear-thinning behavior of the inks crucial to its extrusion from the nozzle, but also its viscoelastic properties to ensure post-printing structure maintenance (Rau et al., 2023; Yuan et al., 2025). To deeply comprehend the rheological behavior of the optimal hydrogels, oscillatory frequency sweep analyses were conducted to characterize their viscoelastic properties by evaluating the G' (storage modulus) and G'' (loss modulus) at 25°C (Fig. 4) and 37°C (SM_4). Concerning Ink_{11} and Ink_{20}, the G' and G'' increased with an increase in the angular frequency (ω) for both inks at 25 °C, showing higher G' and G'' moduli for Ink_{20} (Fig. 4B_1 and B2). This may suggest that increasing the amount of ZnO and/or HPC resulted in higher G' and G'' values. A similar trend was observed when the experiments were conducted at 37°C (SM_4A_1 and A_2). Additionally, for both inks, the G'' was higher than the G', indicating the presence of a liquid-like behavior, until a ω of 71 rad/s for Ink_{11} and 43 rad/s for Ink_{20} at 25°C (Fig. 4B_1 and B_2). At this point, where the G' crossovers the G'' occur, it is possible to observe a transition of the viscoelastic properties that reflects the ink's intrinsic structure from liquid-like (G'<G'') to a predominant elastic behavior (G'>G''). In Fig. 4B3 and B4, regarding the filling hydrogels (Ink_{Alg} and Ink_{OCT}), it was possible to observe that the G' was always higher than the G'', meaning that the ink presents a predominant elastic behavior (solid-like), which is critical to ensure that the filling is maintained inside the macropore after printing (Rau et al., 2023; Yuan et al., 2025). Increasing the angular frequency (ω) resulted in successive increases in both the storage modulus (G′) and loss modulus (G″), while maintaining the material's solid-like behavior. The constancy between G' and G'' as ω increases highlights the stability of the produced inks. Comparable results were also obtained when the rheological evaluation was performed at 37°C (SM_4, A_3 and A_4). Increasing the temperature of Ink_{OCT} from 25°C to 37°C did not change the viscoelastic properties of the ink, since both moduli (G' and G'') did not overlap with each other, maintaining a solid-like behavior. In the Ink_{Alg}, the rise of temperature from 25 °C to 37°C resulted in a lower magnitude of G' and G'', keeping their relative amplitude and preserving the solid-like behavior of the ink, as typically observed in gel formulations (Fig. 4B_3 and SM_4A_3). Fig. 4C_1 and 4C_2 show the evolution of the loss tangent (tan δ) as a function of time for the matrix and filling inks, respectively. For the matrix inks, it was possible to see the transition from liquid (tan δ > 1) to solid-like (tan δ < 1) behavior around 300 s and 323 s, for Ink_{11} and Ink_{20}, respectively (Fig. 4C_1). Nevertheless, increasing the temperature slightly decreased the tan δ, and the time for this transition in both inks (Fig. 4C_1 and SM_4B_1). Furthermore, both filling inks exhibited an almost constant tan δ value, which remained below 1 throughout the test up to 340 s. Beyond this point, tan δ decreased rapidly (Fig. 4C_2).

3.2.3. Antimicrobial and antibiofilm activity

The antimicrobial susceptibility of the printed dressings was tested towards *S. aureus,* one of the most common microorganisms associated with wound infection (Roy et al., 2020).

The minimum inhibitory concentration (MIC) and minimum bactericidal concentration (MBC) of free octenidine were determined as 1–2 μg mL^{-1} and 4 μg mL^{-1}, respectively. In contrast, the MIC of free zinc oxide was found to be 64 mg mL^{-1} (Fig. 5A). Similar MIC values (2 μg mL^{-1}) have been observed for OCT when tested against *S. aureus*, while a MIC value of 34 mg mL^{-1} has been reported for ZnO (Pasquet et al., 2014; Koburger et al., 2010).

To evaluate the antimicrobial susceptibility of the printed dressings, a diffusion agar test was conducted (Fig. 5B_1 and B_2). Furthermore, for control purposes, a drug-free gel (Ink_{Alg}) was used as a filling control of wound dressings (ALG-WD_{11} and ALG-WD_{20}). According to the results, and excluding WD_{11}, all printed dressings presented antimicrobial activity that was possible to identify through the formation of an inhibition halo. Not only did the OCT-loaded dressings presented antimicrobial activity, but also the drug-unloaded samples integrating ZnO at 20 % (w/v). OCT-WD_{20} dressings showed an inhibition halo (1.46 ± 0.17 mm) higher than the OCT disk (0.92 ± 0.07) even though the OCT concentration was similar (≈ 30 μg). This can probably be explained by the inherent antimicrobial activity of the ZnO against *S. aureus* (Babayevska et al., 2022). These findings suggest that the antimicrobial potential of the OCT-WD_{20} is not only attributed to the OCT but also to ZnO, showing a combined effect. The ZnO antimicrobial activity has been reported and attributed to different mechanisms, including ROS generation, release of Zn^{2+}, and its potential to interact directly with the cellular membrane, crossing it and leading to the disruption of cellular processes resulting in the microorganism death (Su et al., 2019; Yang et al., 2022). This was also observed by Pasquet *et al*, when studying different ZnO suspensions with concentrations ranging from 10 to 100 mg/g. The diffusion assay revealed antimicrobial activity against *S. aureus* for all tested samples, with inhibition zone diameters increasing in a concentration-dependent manner (Pasquet et al., 2014).

Antibiofilm activity against *S. aureus* was also tested (Fig. 5C) since the presence of biofilm has been reported as one of the major problems that impairs the healing process, leading to the formation of chronic wounds (Roy et al., 2020). According to the results, the dressings loaded with OCT (OCT-WD_{11} and OCT-WD_{20}) revealed a biofilm decrease of ≈75 % and ≈77 %, respectively. Regarding the dressings printed with Ink_{11}, the only ones that presented antibiofilm activity were the ones loaded with Ink_{OCT}. Results suggest that Ink_{11} did not present antibiofilm properties under the tested conditions. However, when printing with Ink_{20}, all dressings presented antibiofilm activity, including the

A

	MIC (μg/mL)	MBC (μg/mL)
Octenidine	1-2	4
ZnO	64000	-

B1

Sample	Halo (mm)
$Disk_{OCT}$	0.92±0.07
WD_{11}	0
$ALG\text{-}WD_{11}$	0.78±0.29
$OCT\text{-}WD_{11}$	0.89±0.13
WD_{20}	0.84±0.12
$ALG\text{-}WD_{20}$	1.00±0.31
$OCT\text{-}WD_{20}$	1.46±0.17

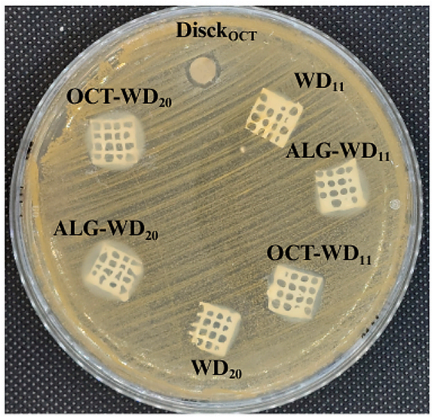

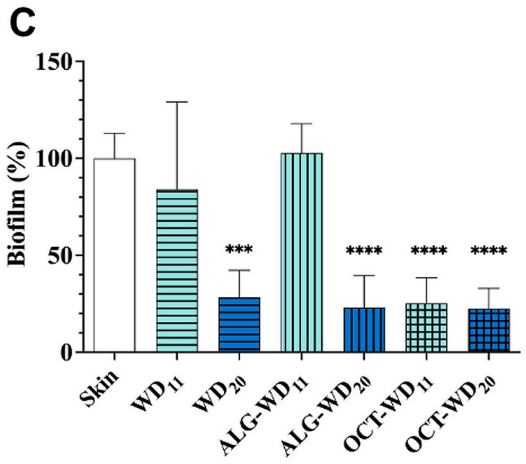

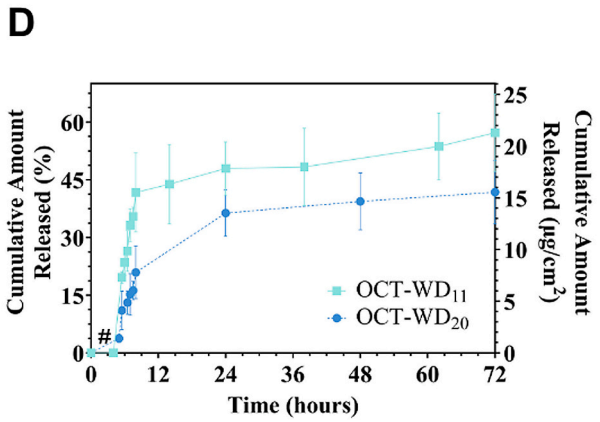

Fig. 5. Activity evaluation of produced dressings. A. Minimum Inhibition Concentration (MIC) and Minimum Bactericidal Concentration (MBC) for OCT and ZnO. B. Antibacterial activity of all printed dressings against *S. aureus* assessed by the agar diffusion assay: inhibition zone diameters (mean ± SD, mm) (B_1) and a representative photograph of the agar plate (B_2). C Antibiofilm activity of the printed dressings against *S. aureus*. ***$p < 0.001$ and **** $p < 0.0001$ when comparing to skin. D. OCT release assay. # lower than the limit of detection.

drug-free. The relationship between the presence of ZnO and antibiofilm activity can be found in the literature, typically relating to the use of ZnO nanoparticles (NPs). For instance, a study performed by Kahandal *et al.* reported ZnO NPs antibiofilm activity against *S. aureus* in a concentration-dependent manner, achieving the highest biofilm inhibition of 61.36 % when using the produced ZnO NPs at 500 μg/mL (Kahandal et al., 2023).

The role of OCT as an antibiofilm drug was undoubtedly confirmed, since the unloaded dressings with Ink_{11} did not present antibiofilm activity, and when OCT was loaded into the macropores, it led to the appearance of activity. Although the contribution of OCT to biofilm reduction in $OCT\text{-}WD_{20}$ could not be conclusively confirmed, the reduction in biofilm formation observed with WD_{20} was a noteworthy finding, as it demonstrated antibiofilm activity without the incorporation of additional bioactive compounds.

3.2.4. *OCT in vitro release*

As shown in Fig. 5D, after 72 h, a higher cumulative drug release from the $OCT\text{-}WD_{11}$ dressing was observed compared with the $OCT\text{-}WD_{20}$ dressing, corresponding to 57 ± 10 % and 42 ± 8 %. Drug loading was determined by assuming that the OCT concentration in the alginate hydrogel ink corresponded to the value obtained by UV–Vis spectrophotometry. The total amount of OCT loaded into the alginate hydrogel was found to be 0.092 %, which is slightly lower than the theoretical loading of 0.1 % (w/v).

For both dressings, the OCT release could only be detected after 5.5 h, since drug concentrations were below the limit of detection of the method (0.015 μg/mL). A burst phase was observed between 5.5 and 8 h, reaching a release of 42 ± 10 % and 21 ± 7 %, for $OCT\text{-}WD_{11}$ and $OCT\text{-}WD_{20}$, respectively. At 24 h, more than 45 % of the drug was released from the $OCT\text{-}WD_{11}$ dressing (48 ± 7 %). Moreover, OCT concentrations exceeding the minimum inhibitory concentration (MIC, 1–2 μg mL^{-1}) were quantified after 6 h for both $OCT\text{-}WD_{11}$ and $OCT\text{-}WD_{20}$. Comparing the two dressings, a trend could be observed between the amount of ZnO used to print the dressings (11 vs. 20 %) and the concentration of drug released, with higher ZnO content resulting in lower OCT release. The lower drug release from $OCT\text{-}WD_{20}$ may be explained by the reduced capacity of the solvent to access and dissolve OCT within the matrix, due to the concomitant solubilization of high amounts of ZnO in the delivery system and a resulting solvent saturation effect (Siepmann and Siepmann, 2020).

To understand the mechanism of OCT release, data were fitted to a well-established mathematical model, the Korsmeyer-Peppas (KP, $\frac{Q_t}{Q_\infty} = K_k t^n$) (Costa and Sousa Lobo, 2001), presenting an R^2 of 0.988 and 0.886 for $OCT\text{-}WD_{11}$ and $OCT\text{-}WD_{20}$, respectively. According to the KP model, the parameter *n* is used to characterize the type of mechanism related to the drug release from the dressings' polymeric matrix (Costa and Sousa Lobo, 2001). Both dressings presented an $n > 1$ (2.00 for $OCT\text{-}WD_{11}$ and 2.97 for $OCT\text{-}WD_{20}$), characterized by a super case II transport (Costa and Sousa Lobo, 2001). Hence, the OCT release is not exclusively influenced by diffusion mechanisms through the dressings, but also by the swelling and relaxation of the Alg:ZnO:HPC matrix and its

breakdown will be determinant for the drug release (Siepmann and Peppas, 2001; Karnik et al., 2025).

At this stage, one hypothesis can be proposed: the lower amount of OCT released after 24 h from the formulation containing 20 % (w/v) of ZnO may explain the similar antibiofilm activities observed for WD_{20} and OCT-WD_{20}. Results suggest that the amount of OCT released from the OCT-WD_{20} sample was not enough to observe an increase in antibiofilm activity as expected.

The unreleased fraction of OCT is likely retained within the alginate/ZnO matrix due to diffusion limitations and drug–matrix interactions. In fact, alginate-based crosslinked hydrogels are known to retain a portion of the loaded drug as a result of matrix entrapment, restricted diffusional transport, and physicochemical interactions between the drug and the polymer network (Lin et al., 2019). Consequently, release studies do not necessarily recover 100 % of the initially loaded drug, particularly in highly crosslinked systems where a fraction of the payload may remain associated with the matrix even after prolonged release periods.

3.2.5. *In vitro cytocompatibility and evaluation of the regenerative potential*

In addition to antibacterial activity, dressing materials must be biocompatible for wound-healing applications. To evaluate their *in vitro* cytocompatibility and regenerative potential, an indirect culture setting was employed. Porous inserts with the developed dressings were mounted in culture wells, allowing the diffusion of soluble components into the human dermal fibroblast cultures. This indirect exposure model is widely used for biomaterial cytocompatibility screening, as it evaluates the biological effects of released compounds while preserving monolayer integrity and avoiding artefacts associated with direct material contact, such as mechanical disturbance or heterogeneous cell–material interactions (Pimton et al., 2022). The structural stability of the dressings during 24 h of incubation in culture medium at 37°C and buffered pH ensured consistent leachate exposure, supporting a reliable cytocompatibility assessment and confirming adequate physiological stability.

As shown in Fig. 6A and B, HDF cultures exposed to the dressing leachates displayed metabolic activity and LDH release comparable to the control, indicating a cytocompatible profile. All experimental groups demonstrated a trend toward enhanced metabolic activity, with WD_{11} and WD_{20} showing a statistically significant increase compared with the control. These findings support the biological compatibility of the developed matrices and suggest a stimulatory effect associated with Zn-containing formulations. The observed metabolic enhancement is

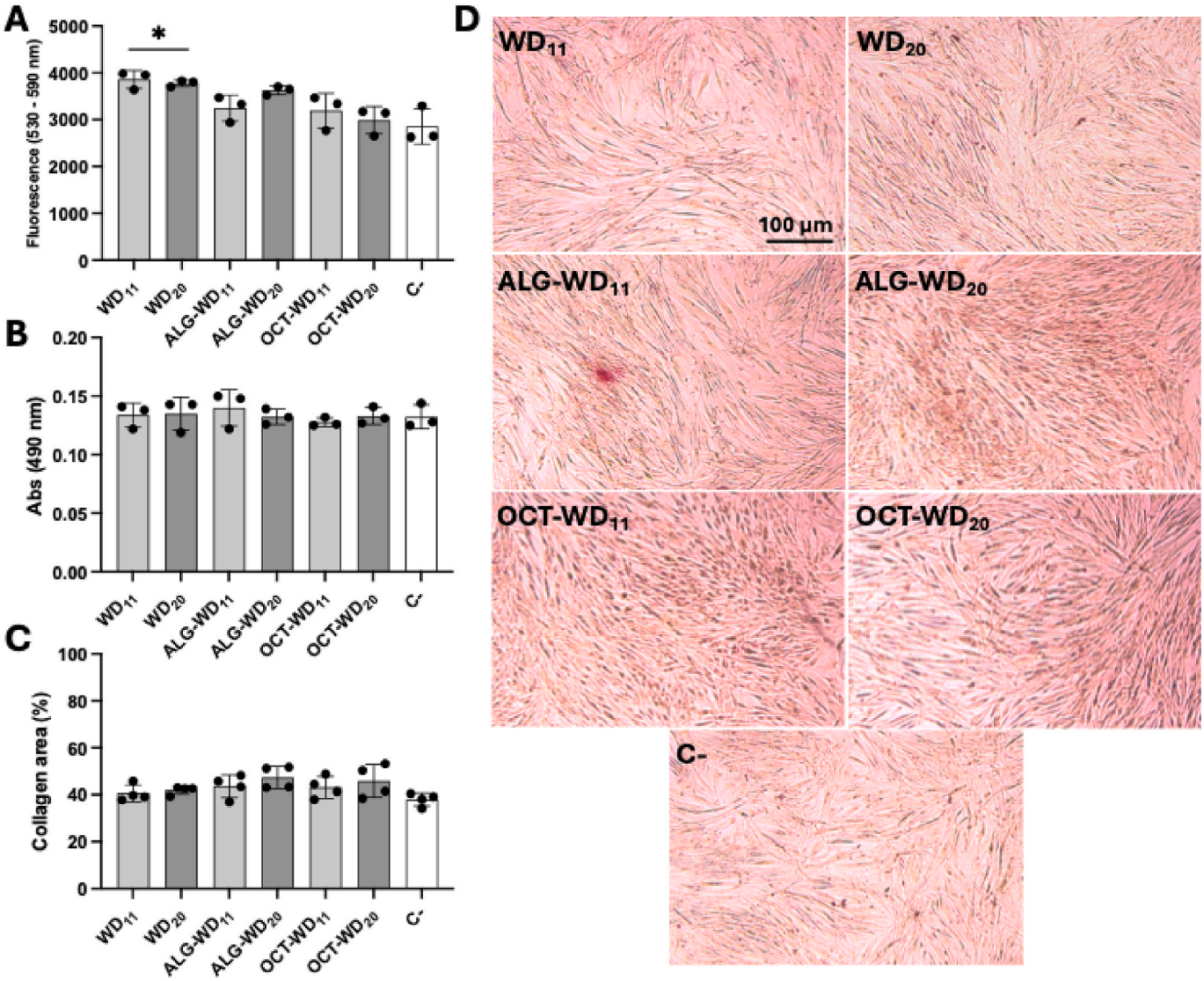

Fig. 6. *In vitro* cytocompatibility assessment of the printed dressings with human dermal fibroblasts, after 24 h of incubation. A. Metabolic activity quantification by the resazurin assay. B. Lactate dehydrogenase (LDH) release. C. Semi-quantitative analysis of collagen deposition following Sirius Red staining. D. Representative microscopy images of Sirius-Red-stained fibroblast cultures. * Significantly different from control (C-), $p < 0.05$.

consistent with the known role of Zn^{2+} ions in modulating fibroblast function (Ma et al., 2024; Shao et al., 2025), particularly through the promotion of cell adhesion, spreading, and proliferative activity within regenerative microenvironments. The cytocompatibility of the single materials herein used has been demonstrated across some wound dressings, and increased cellular metabolic activity has been observed in a wide range of ZnO concentrations, as released zinc ions can enhance cell adhesion and proliferation (Ma et al., 2024; Wiesmann et al., 2021).

Regarding OCT-containing formulations (OCT-WD_{11}, OCT-WD_{20}), cytocompatibility results should be interpreted in light of the known biological profile of this antiseptic. Its cationic character is known to induce marked dose-dependent cytotoxicity, although the reported cytotoxic concentrations vary according to the biological system, cell population and exposure conditions (Cai et al., 2023; Mattar et al., 2025; Abdel-Rahman et al., 2024). Based on the OCT content per sample, the highest release measured after 24 h and the culture-medium volume, the nominal OCT concentration in the present assay was estimated as 13.2 μg/mL. This value was substantially below the IC_{50} reported in one study (Cai et al., 2023), but within the concentration range associated with cytotoxic effects in other cellular models (Mattar et al., 2025), further highlighting the influence of the experimental system. Importantly, previous work reported cytotoxicity following direct exposure to free OCT, whereas exudates from OCT-loaded dressings preserved cell viability (Mattar et al., 2025). In the present study, OCT-containing formulations did not alter metabolic activity or LDH release relative to unloaded counterparts, indicating preserved cytocompatibility under the tested indirect-exposure conditions. These findings suggest that the formulation and mode of exposure influence the biological response to OCT. Nevertheless, because the OCT concentration and freely bioavailable fraction in the culture medium were not directly measured, the preserved cytocompatibility cannot be specifically attributed to controlled release.

Considering collagen deposition, all experimental groups exhibited levels comparable to the control (Fig. 6C and D), with a trend toward a modest increase in the alginate-based formulations. This trend may be related to the known ability of alginate matrices to support fibroblast activity and extracellular matrix deposition, including collagen synthesis (Porrelli et al., 2021). Collagen is a key structural component of the extracellular matrix (ECM) and plays a critical role in the wound-healing process, serving as a template for cell migration and tissue remodeling (Zheng et al., 2022). Consequently, its deposition is indicative of a preserved fibroblast function and supports an adequate healing response, further indicating the suitability of the developed dressings, including those loaded with OCT.

Wound closure represents a pivotal stage in tissue repair. The *in vitro* scratch assay is widely employed to evaluate cell proliferation and migration due to its straightforward execution, reproducibility, and cost-effectiveness (Chen et al., 2019). As shown in Fig. 7, the control and experimental groups exhibited similar wound closure at 24 h, with evident spaces between the migrating cells. At 48 h, wound closure exceeded 80 % in all groups, with the WD_{11}, ALG-WD_{11}, WD_{20}, and ALG-WD_{20} groups achieving approximately complete closure, demonstrating a significant improvement compared with the control and OCT-loaded groups.

These findings highlight the regenerative potential of the developed ZnO–alginate matrices for wound-healing applications (Ma et al., 2024;

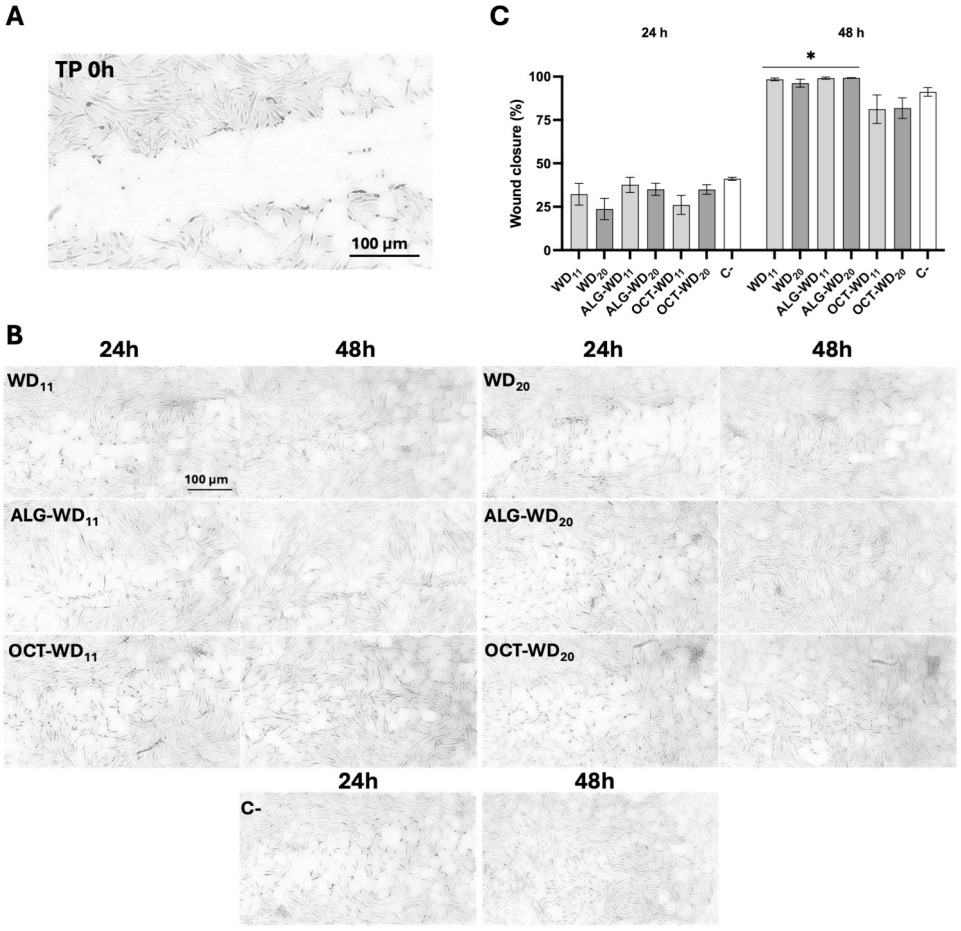

Fig. 7. *In vitro* scratch assay in human dermal fibroblasts exposed to the printed dressings. A. Representative microscopy image of the cell monolayer immediately after scratching. B. Representative microscopy images of control and experimental groups at 24 and 48 h. C. Semi-quantitative analysis of wound closure. * Significantly different from control (C-) at 48 h, $p < 0.05$.

Shao et al., 2025). The improved performance may be attributed to zinc's biological activity in modulating oxidative balance and inflammatory signaling, including the neutralization of reactive oxygen species (ROS) and excessive pro-inflammatory responses, ultimately preserving cellular integrity within the wound environment (Martin et al., 2024; Tayyeb et al., 2024). Furthermore, Zn ion release can promote fibroblast attachment and proliferation, thereby accelerating the healing process (Ma et al., 2024; Shao et al., 2025). OCT-loaded groups showed performance similar to the control, indicating satisfactory healing potential, although slightly lower than that of the unloaded formulations, just at 48 h. This difference may reflect cumulative OCT exposure in the culture medium at 48 h, which can impact HDF migration and proliferation, whereas *in vivo*, fluid turnover and tissue clearance would likely prevent local accumulation (Rakkan et al., 2024). Nonetheless, all experimental groups demonstrated adequate *in vitro* healing performance, supporting their progression toward *in vivo* biocompatibility assessment.

3.2.6. *In vivo biocompatibility*

The *in vivo* biocompatibility of the printed dressings was evaluated through subcutaneous implantation for 7 and 15 days (Figs. 8 and 9). This model enabled assessment of the short-term local tissue response under physiological conditions, complementing the rheological characterization performed at 37°C. At day 7, all dressing formulations were detectable as non-staining structures with noticeable areas of structural disassembly, indicating early structural fragmentation. A thin, fibrous capsule composed predominantly of collagen fibers oriented parallel to the implant surface was observed surrounding all materials, indicating an early maturation phase of the *peri*-implant interface. Additionally, the capsule was encircled by numerous spindle-shaped fibroblastic cells with elongated nuclei, newly formed blood capillaries indicative of early vascularization, and scattered mononuclear inflammatory infiltrate. These features are consistent with a controlled foreign-body reaction associated with mild chronic inflammation and ongoing physiological tissue repair, supporting a favorable early host-tissue tolerance profile. Importantly, no microabscesses, necrotic foci, or acute suppurative inflammation were identified. Comparative histological evaluation revealed no discernible differences among the various dressing formulations, regardless of ZnO concentration or the presence of ALG or OCT, supporting a comparable early biocompatibility profile across all tested materials.

At day 15, the printed dressings remained detectable in the subcutaneous tissue, with no clear evidence of cellular colonization. However, they appeared more fragmented and discontinuous, with additional fibrotic compartments, indicating progressive structural disassembly. The fibrous capsule was notably thicker and more organized, with densely packed collagen layers and reduced cellularity and neovascularization compared to day 7. Inflammatory cells were sparse to nearly absent, indicating a diminished – and in most areas near resolved – inflammatory response, consistent with a progression toward tissue remodeling and ongoing repair, and supporting good host tissue tolerance to the degrading material.

These findings demonstrate the favorable *in vivo* biocompatibility of the developed zinc-alginate-based dressings, which exhibit high biocompatibility upon subcutaneous implantation, typically eliciting only minimal-to-mild inflammatory responses without evidence of necrosis or systemic toxicity (Bar-Shai et al., 2025; Kumar et al., 2023). Although the increased fragmentation observed between days 7 and 15 suggests progressive structural disassembly, the present short-term histological evaluation was not designed to determine degradation kinetics

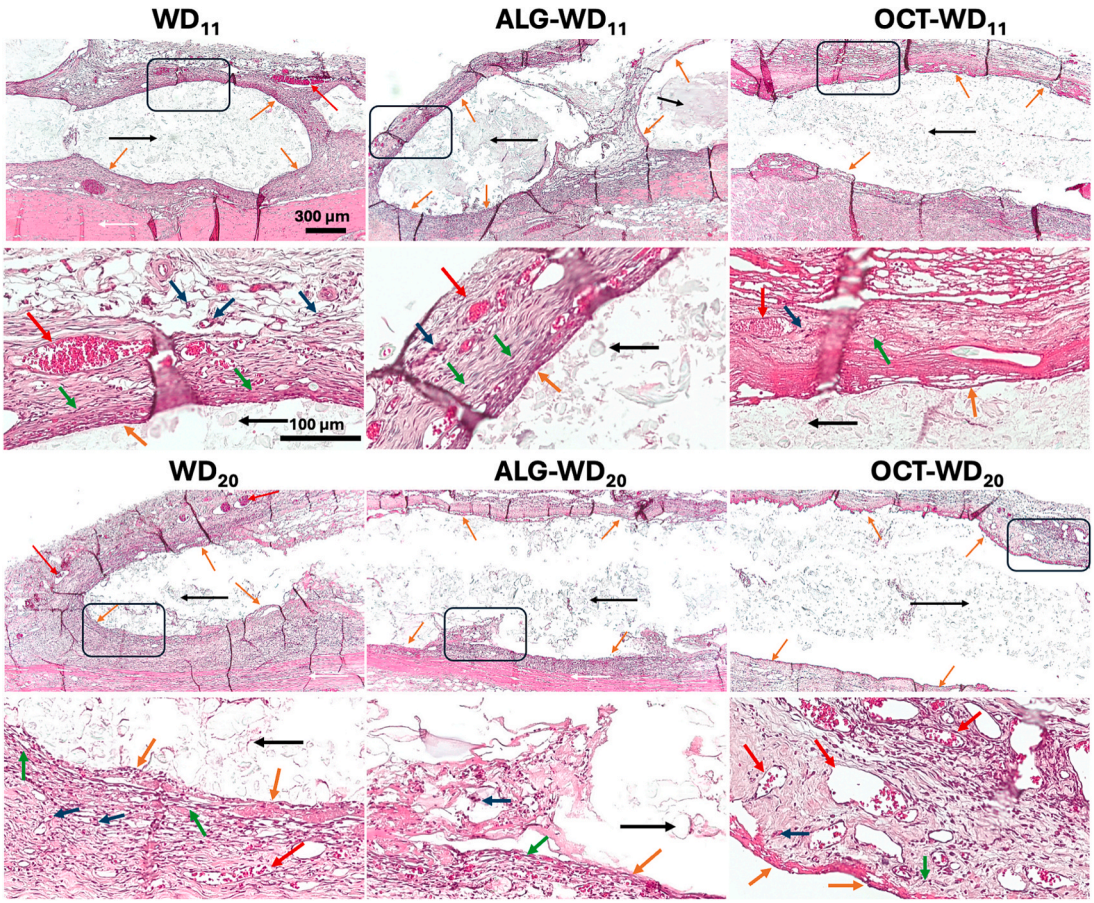

Fig. 8. *In vivo* biocompatibility assessment. Representative histological images of subcutaneous implantation sites after 7 days, stained with H&E. Red arrow – Blood vessels; Orange arrow – Fibrous capsule; Black arrow – Implanted dressings; Blue arrow – Macrophages; Green arrow – Fibroblasts; White arrow – Muscle tissue.

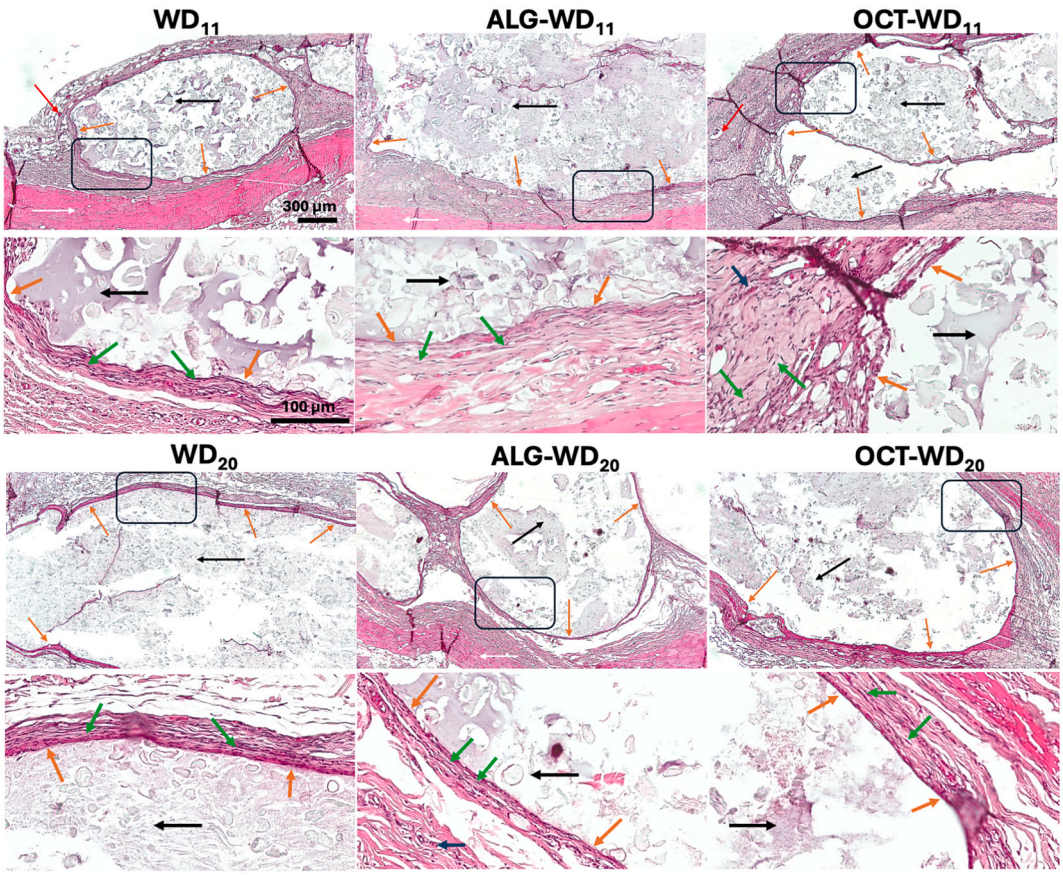

Fig. 9. *In vivo* biocompatibility assessment. Representative histological images of the subcutaneous implantation site after 15 days, stained with H&E. Red arrow – Blood vessels; Orange arrow – Fibrous capsule; Black arrow – Implanted dressings; Blue arrow – Macrophages; Green arrow – Fibroblasts; White arrow – Muscle tissue.

or complete material resorption. Notably, the incorporation of OCT did not alter the host response compared to unloaded dressings, supporting the *in vivo* biocompatibility of the cationic antiseptic within the developed platform. The superior biocompatibility index of OCT, relative to conventional antiseptics, such as cetylpyridinium chloride and chlorhexidine, likely underpins the favorable histological outcomes observed in the present study (Mattar et al., 2025; Muller and Kramer, 2008).

4. Conclusions

An innovative wound dressing platform was successfully developed through 3D printing with unique regenerative and healing inks that integrate alginate, ZnO, and HPC. Overall, this study also provides proof-of-concept that the produced regenerative dressings are suitable for further drug loading, assuring therapeutic customization when needed.

Suitable printable inks were achieved with HPC supplementation, showing a positive impact on the printing performance, fitting a shear-thinning behavior, and a final product close to the theoretical digital model. Developed dressings demonstrated consistent cytocompatibility in both *in vitro* and *in vivo* models, with metabolic activity, LDH release, and host response comparable to those in control conditions. Additionally, their regenerative potential was further supported by comparable collagen deposition and wound-closure performance, with wounds achieving near-complete closure within 48 h. Incorporation of a model drug, i.e., octenidine, within the dressing pores provided antibacterial and antibiofilm activity to the loaded dressings, and the drug release profile over time was consistent with a specific release model. Moreover, OCT-loaded dressings preserved the biocompatibility of the drug-free formulations, supporting both their capacity to incorporate active compounds within their pores and their biological suitability as a promising platform for advanced wound management.

The study demonstrated the potential of using a semi-solid extrusion 3D printing technology to produce dressings intended for chronic wounds that can also be customized by changing the dressing's conformation or by incorporating active compounds according to the patient's needs.

Ethics declaration

CRediT authorship contribution statement

Sara Cardoso: Writing – original draft, Methodology, Investigation, Formal analysis. **Victor Martin:** Writing – original draft, Methodology, Investigation, Formal analysis. **Catarina Leal:** Writing – review & editing, Validation, Resources, Methodology. **Nuno Monge:** Visualization. **Bruno Colaço:** Methodology, Investigation. **Pedro Gomes:** Writing – review & editing, Validation, Methodology. **Ana F. Bettencourt:** Writing – review & editing, Validation, Supervision, Methodology. **Isabel A.C. Ribeiro:** Writing – review & editing, Visualization, Validation, Supervision, Resources, Project administration, Methodology, Funding acquisition, Conceptualization.

This study was conducted in accordance with the ARRIVE (Animal Research: Reporting of In Vivo Experiments) guidelines. This study was approved by the UTAD Local Committee Responsible for animal welfare. (Approval No. DGAV 36606/25-S).

Declaration of competing interest

The authors declare that they have no known competing financial

interests or personal relationships that could have appeared to influence the work reported in this paper.

Acknowledgements

The authors would like to thank Fundação para a Ciência e Tecnologia / Ministério da Educação, Ciência e Inovação (FCT/MECI), Portugal, for financial support from: i) Project 15980 (COMPETE2030-FEDER-00711700, LISBOA2030-FEDER-00711700, reference: 2023.16511.ICDT (https://doi.org/10.54499/2023.16511.ICDT); ii) Instituto de Investigação do Medicamento (iMed.ULisboa), Project UID/04138/2025 (DOI:10.54499/UID/04138/2025); iii) Laboratório Associado para a Química Verde - Tecnologias e Processos Limpos Project UID/50006/2025 (DOI: 10.54499/UID/50006/2025); iv) S. Cardoso PhD Grant 2023.01295.BDANA (DOI:10.54499/2023.01295.BDANA). The authors also acknowledge the support of the i3S Scientific Platforms HEMS-Histology and Electron Microscopy Department.

Appendix A. Supplementary data

Supplementary data to this article can be found online at https://doi.org/10.1016/j.ijpharm.2026.127356.

Data availability

Data will be made available on request.

References

Falanga, V., Isseroff, R.R., Soulika, A.M., Romanelli, M., Margolis, D., Kapp, S., Granick, M., Harding, K., 2022. Chronic wounds. Nat. Rev. Dis. Prim. 8, 50. https://doi.org/10.1038/s41572-022-00377-3.

Las Heras, K., Igartua, M., Santos-Vizcaino, E., Hernandez, R.M., 2020. Chronic wounds: current status, available strategies and emerging therapeutic solutions. J. Control. Release 328, 532–550. https://doi.org/10.1016/j.jconrel.2020.09.039.

Shukla, A.K., Ahn, M., Gao, J., Lee, D., Yoon, S., Oh, S.-O., Gao, G., Cho, W.-W., Kim, B.S., 2026. Exploring the angiogenic potential of skin patches with endothelial cell patterns fabricated via in-bath 3D bioprinting using light-activated bioink for enhanced wound healing. Biomaterials 325, 123575. https://doi.org/10.1016/j.biomaterials.2025.123575.

Zhou, X., Yu, X., You, T., Zhao, B., Dong, L., Huang, C., Zhou, X., Xing, M., Qian, W., Luo, G., 2024. 3D printing-based hydrogel dressings for wound healing. Adv. Sci. 11, doi:10.1002/advs.202404580.

Fan, C., Xu, Q., Hao, R., Wang, C., Que, Y., Chen, Y., Yang, C., Chang, J., 2022. Multifunctional wound dressings based on silicate bioactive materials. Biomaterials 287, 121652. https://doi.org/10.1016/j.biomaterials.2022.121652.

Zöller, K., To, D., Bernkop-Schnürch, A., 2025. Biomedical applications of functional hydrogels: innovative developments, relevant clinical trials and advanced products. Biomaterials 312, 122718. https://doi.org/10.1016/j.biomaterials.2024.122718.

Chen, X., Zhou, Y., Zhou, S., Zhang, D., Zeng, L., Zhou, C., Liu, M., 2025. 3D printing of chitosan hydrogel reinforced with tubular nanoclay for hemostasis and infected wound healing. Bioact. Mater. 54, 404–422. https://doi.org/10.1016/j.bioactmat.2025.08.024.

Kim, H.S., Lee, I.Y., Hwang, J., Park, J.S., Kim, Y., Lee, K.Y., 2026. 3D-printable hyaluronic acid/gelatin double-network hydrogels for stretchable and adhesive wound patches. Int. J. Biol. Macromol. 343, 150392. https://doi.org/10.1016/j.ijbiomac.2026.150392.

Lin, K., Xu, H., Liu, H., Jiang, H., Mei, H., Jiang, L., Du, Z., Tan, W., Li, X., Zhou, J., et al., 2026. Bioprinted dressing with symbiotic microbes for oxygen supply and antibacterial therapy for enhanced diabetic wound healing. J. Control. Release 114653, doi:10.1016/j.jconrel.2026.114653.

Teoh, J.H., Tay, S.M., Fuh, J., Wang, C.-H., 2022. Fabricating scalable, personalized wound dressings with customizable drug loadings via 3D printing. J. Control. Release 341, 80–94. https://doi.org/10.1016/j.jconrel.2021.11.017.

Umoren, S.A., Solomon, M.M., Saji, V.S., 2022. Alginate and its derivatives. In: Polymeric Materials in Corrosion Inhibition. Elsevier, pp. 271–286.

Paques, J.P., van der Linden, E., van Rijn, C.J.M., Sagis, L.M.C., 2014. Preparation methods of alginate nanoparticles. Adv. Colloid Interface Sci. 209, 163–171. https://doi.org/10.1016/j.cis.2014.03.009.

Mallakpour, S., Azadi, E., Hussain, C.M., 2021. State-of-the-art of 3D printing technology of alginate-based hydrogels—an emerging technique for industrial applications. Adv. Colloid Interface Sci. 293, 102436. https://doi.org/10.1016/j.cis.2021.102436.

Sharma, A., Verma, C., Singh, P., Mukhopadhyay, S., Gupta, A., Gupta, B., 2024. Alginate based biomaterials for hemostatic applications: innovations and developments. Int. J. Biol. Macromol. 264, 130771. https://doi.org/10.1016/j.ijbiomac.2024.130771.

Mazurek, Ł., Kuś, M., Jurak, J., Rybka, M., Kuczeriszka, M., Stradczuk-Mazurek, M., Konop, M., 2025. Biomedical potential of alginate wound dressings – from preclinical studies to clinical applications: a review. Int. J. Biol. Macromol. 309, 142908. https://doi.org/10.1016/j.ijbiomac.2025.142908.

Rahaman, M.S., Arin, A., Farwa, U., Park, M., Bae, S.H., Lee, B.-T., 2024. ECM derivatized alginate augmenting bio-functionalities of lyophilized mat for skin and liver wound treatment. Biomaterials 311, 122698. https://doi.org/10.1016/j.biomaterials.2024.122698.

Barsky, D., Ben Ya'acov, A., Avraham, L.W., Nachman, D., Eisenkraft, A., Mintz, Y., Shteyer, E., 2022. A feasibility study using sodium alginate injection for penetrating abdominal trauma in a swine model. Sci. Rep. 12, 17132. https://doi.org/10.1038/s41598-022-22186-0.

Su, Y., Cockerill, I., Wang, Y., Qin, Y.-X., Chang, L., Zheng, Y., Zhu, D., 2019. Zinc-based biomaterials for regeneration and therapy. Trends Biotechnol. 37, 428–441. https://doi.org/10.1016/j.tibtech.2018.10.009.

Yang, N., Venezuela, J., Almathami, S., Dargusch, M., 2022. Zinc-nutrient element based alloys for absorbable wound closure devices fabrication: current status, challenges, and future prospects. Biomaterials 280, 121301. https://doi.org/10.1016/j.biomaterials.2021.121301.

Fang, W., Yang, M., Wang, L., Li, W., Liu, M., Jin, Y., Wang, Y., Yang, R., Wang, Y., Zhang, K., et al., 2023. Hydrogels for 3D bioprinting in tissue engineering and regenerative medicine: current progress and challenges. Int. J. Bioprinting 9, 759. https://doi.org/10.18063/ijb.759.

Vajda, J., Bjelić, D., Vihar, B., Vesenjak, M., Dubrovski, P.D., Gradišnik, L., Belak, M., Maver, U., Milojević, M., 2025. 3D printed fibroblast-laden alginate-cellulose scaffolds support extracellular matrix formation and angiogenic growth factor secretion. Int. J. Biol. Macromol. 332, 148701. https://doi.org/10.1016/j.ijbiomac.2025.148701.

Torres-Ayala, L.K., Nakamatsu, J., Kim, S., 2025. Rheological optimization of hybrid alginate–xanthan gum hydrogels for enhanced 3D bioprinting fidelity. Polym. Bull. 82, 9947–9976. https://doi.org/10.1007/s00289-025-05923-z.

Cardoso, S., Martin, V., Pereira, J.C., David, A.B., Araújo, R., Gonçalves, L., Landin, M., Gomes, P., Ferraz, M.P., Ribeiro, I.A.C., et al., 2025. 3D-printed chitosan-starch mesh filled with minocycline-alginate hydrogel for dual anti-staphylococcus aureus and osteogenic effects. Carbohydr. Polym. 370, 124311. https://doi.org/10.1016/j.carbpol.2025.124311.

Ahmadi Soufivand, A., Faber, J., Hinrichsen, J., Budday, S., 2023. Multilayer 3D bioprinting and complex mechanical properties of alginate-gelatin mesostructures. Sci. Rep. 13, 11253. https://doi.org/10.1038/s41598-023-38323-2.

Yalman, V., Türkoğlu, N., Şahin, Y.M., 2025. Development of gelatine and alginate based inks for 3D bioprinters and characterization. Int. J. Biol. Macromol. 295, 139666. https://doi.org/10.1016/j.ijbiomac.2025.139666.

Silva, D.J., Michelini, G.S., de Sá, R.C.L., Ferreira, A.H., 2025. Unveiling linear and nonlinear viscoelastic fingerprints of CMC/alginate polysaccharide hydrogels via FT-rheology: implications for advanced 3D printing. Carbohydr. Polym. 124598, doi:10.1016/j.carbpol.2025.124598.

Gan, S., Bai, S., Chen, C., Zou, Y., Sun, Y., Zhao, J., Rong, J., 2021. Hydroxypropyl cellulose enhanced ionic conductive double-network hydrogels. Int. J. Biol. Macromol. 181, 418–425. https://doi.org/10.1016/j.ijbiomac.2021.03.068.

Ouyang, L., Yao, R., Zhao, Y., Sun, W., 2016. Effect of bioink properties on printability and cell viability for 3D bioplotting of embryonic stem cells. Biofabrication 8, 035020. https://doi.org/10.1088/1758-5090/8/3/035020.

Cardoso, S., Narciso, F., Monge, N., Bettencourt, A., Ribeiro, I.A.C., 2023. Improving chitosan hydrogels printability: a comprehensive study on printing scaffolds for customized drug delivery. Int. J. Mol. Sci. 24. https://doi.org/10.3390/IJMS24020973.

Narciso, F., Cardoso, S., Monge, N., Lourenço, M., Martin, V., Duarte, N., Santos, C., Gomes, P., Bettencourt, A., Ribeiro, I.A.C., 2023. 3D-printed biosurfactant-chitosan antibacterial coating for the prevention of silicone-based associated infections. Colloids Surf. B Biointerf. 230, 113486. https://doi.org/10.1016/j.colsurfb.2023.113486.

Pontes, C., Alves, M., Santos, C., Ribeiro, M.H., Gonçalves, L., Bettencourt, A.F., Ribeiro, I.A.C., 2016. Can sophorolipids prevent biofilm formation on silicone catheter tubes? Int. J. Pharm. 513, 697–708. https://doi.org/10.1016/j.ijpharm.2016.09.074.

Severo, C., Anjos, I., Souza, V.G.L., Canejo, J.P., Bronze, M.R., Fernando, A.L., Coelhoso, I., Bettencourt, A.F., Ribeiro, I.A.C., 2021. Development of cranberry extract films for the enhancement of food packaging antimicrobial properties. Food Packag. Shelf Life 28, 100646. https://doi.org/10.1016/j.fpsl.2021.100646.

Vieira, P., Bettencourt, A.F., Panteli, E., Santos, C., Gonçalves, L.M., Francisco, A.P., Ribeiro, I.A.C., 2024. Exploring triazene derivative's antimicrobial activity and its incorporation onto 3D-printed coatings. Mater. Today Chem. 38, 102133. https://doi.org/10.1016/j.mtchem.2024.102133.

CLSI Performance Standards for Antimicrobial Disk Susceptibility Tests, 2024. In CLSI standard M02, 14th edition; Clinical and Laboratory Standards Institute.

Mendes, R.M., Francisco, A.P., Carvalho, F.A., Dardouri, M., Costa, B., Bettencourt, A.F., Costa, J., Gonçalves, L., Costa, F., Ribeiro, I.A.C.F., 2021. Fighting *S. aureus* catheter-related infections with sophorolipids: electing an antiadhesive strategy or a release one? Colloids Surf. B Biointerf. 208, 112057. https://doi.org/10.1016/j.colsurfb.2021.112057.

Nobre, D., Ekoh, E., Silva, D.C., Branco, A.C., Pais, V., Almeida, A., Barroso, H., Salema-Oom, M., Fangueiro, R., Colaço, R., et al., 2025. Antimicrobial casein/poly(vinyl alcohol) electrospun nanofibers-based dressings. Int. J. Pharm. 686, 126320. https://doi.org/10.1016/j.ijpharm.2025.126320.

Murab, S., Gupta, A., Włodarczyk-Biegun, M.K., Kumar, A., van Rijn, P., Whitlock, P., Han, S.S., Agrawal, G., 2022. Alginate based hydrogel inks for 3D bioprinting of engineered orthopedic tissues. Carbohydr. Polym. 296, 119964. https://doi.org/10.1016/j.carbpol.2022.119964.

Kong, D., Yang, B., Yuan, H., Du, C., Tan, Y., 2025. 3D printing of glycerol-mediated alginate hydrogels with high strength and stiffness. J. Mater. Sci. Technol. 213, 268–275. https://doi.org/10.1016/j.jmst.2024.07.001.

Rau, D.A., Williams, C.B., Bortner, M.J., 2023. Rheology and printability: a survey of critical relationships for direct ink write materials design. Prog. Mater Sci. 140, 101188. https://doi.org/10.1016/j.pmatsci.2023.101188.

Schwab, A., Levato, R., D'Este, M., Piluso, S., Eglin, D., Malda, J., 2020. Printability and shape fidelity of bioinks in 3D bioprinting. Chem. Rev. 120, 11028–11055. https://doi.org/10.1021/acs.chemrev.0c00084.

Helmiyati, Aprilliza, M., 2017. Characterization and properties of sodium alginate from brown algae used as an ecofriendly superabsorbent. IOP Conf. Ser. Mater. Sci. Eng. 188, 012019. https://doi.org/10.1088/1757-899X/188/1/012019.

Fang, S., Liu, K., Zhou, X., Jin, X., Feng, C., Zhu, Q., Jiang, H., Zhang, P., 2025. Design and evaluation of high-viscosity gelatin / polyacrylamide / sodium alginate triple-network hydrogels for 3D printing: fluid dynamics simulation and experimental method. Int. J. Biol. Macromol. 318, 144886. https://doi.org/10.1016/j.ijbiomac.2025.144886.

Alharbi, N.D., Guirguis, O.W., 2019. Macrostructure and optical studies of hydroxypropyl cellulose in pure and nano-composites forms. Results Phys. 15, 102637. https://doi.org/10.1016/j.rinp.2019.102637.

Halbus, A.F., Athab, Z.H., Mohammed, S.B., Baqir, S.J., 2025. Thermoresponsive and reusable chitosan/hydroxypropyl cellulose monolithic hydrogel with interconnected porosity engineered via freeze–thaw processing for selective dyes removal. Int. J. Biol. Macromol. 333, 148899. https://doi.org/10.1016/j.ijbiomac.2025.148899.

Černá, E., Neděla, V., Tihlařiková, E., Brtníková, J., Fohlerová, Z., Lipový, B., Vacek, L., Růžička, F., Matulová, J., Vojtová, L., 2025. Glycerol-enhanced gum karaya hydrogel films with a sandwich-like structure enriched with octenidine for antibacterial action against multidrug-resistant bacteria. ACS Omega 10, 29530–29546. https://doi.org/10.1021/acsomega.5c02915.

Pan, F., Amarjargal, A., Altenried, S., Liu, M., Zuber, F., Zeng, Z., Rossi, R.M., Maniura-Weber, K., Ren, Q., 2021. Bioresponsive hybrid nanofibers enable controlled drug delivery through glass transition switching at physiological temperature. ACS Appl. Bio Mater. 4, 4271–4279. https://doi.org/10.1021/acsabm.1c00099.

Yuan, Z., Huang, X., Zhang, X., Gao, S., Chen, H., Li, Z., El-Mesery, H.S., Shi, J., Zou, X., 2025. Unveiling rheological behavior of hydrogels toward magic 3D printing patterns. Food Hydrocoll. 168, 111505. https://doi.org/10.1016/j.foodhyd.2025.111505.

Roy, S., Santra, S., Das, A., Dixith, S., Sinha, M., Ghatak, S., Ghosh, N., Banerjee, P., Khanna, S., Mathew-Steiner, S., et al., 2020. *Staphylococcus aureus* biofilm infection compromises wound healing by causing deficiencies in granulation tissue collagen. Ann. Surg. 271, 1174–1185. https://doi.org/10.1097/SLA.0000000000003053.

Pasquet, J., Chevalier, Y., Couval, E., Bouvier, D., Noizet, G., Morlière, C., Bolzinger, M.-A., 2014. Antimicrobial activity of zinc oxide particles on five micro-organisms of the challenge tests related to their physicochemical properties. Int. J. Pharm. 460, 92–100. https://doi.org/10.1016/j.ijpharm.2013.10.031.

Koburger, T., Hubner, N.-O., Braun, M., Siebert, J., Kramer, A., 2010. Standardized comparison of antiseptic efficacy of triclosan, PVP-iodine, octenidine dihydrochloride, polyhexanide and chlorhexidine digluconate. J. Antimicrob. Chemother. 65, 1712–1719. https://doi.org/10.1093/jac/dkq212.

Babayevska, N., Przysiecka, Ł., Iatsunskyi, I., Nowaczyk, G., Jarek, M., Janiszewska, E., Jurga, S., 2022. ZnO size and shape effect on antibacterial activity and cytotoxicity profile. Sci. Rep. 12, 8148. https://doi.org/10.1038/s41598-022-12134-3.

Pasquet, J., Chevalier, Y., Pelletier, J., Couval, E., Bouvier, D., Bolzinger, M.-A., 2014. The contribution of zinc ions to the antimicrobial activity of zinc oxide. Colloids Surf. A Physicochem. Eng. Asp. 457, 263–274. https://doi.org/10.1016/j.colsurfa.2014.05.057.

Kahandal, A., Chaudhary, S., Methe, S., Nagwade, P., Sivaram, A., Tagad, C.K., 2023. Galactomannan polysaccharide as a biotemplate for the synthesis of zinc oxide nanoparticles with photocatalytic, antimicrobial and anticancer applications. Int. J. Biol. Macromol. 253, 126787. https://doi.org/10.1016/j.ijbiomac.2023.126787.

Siepmann, J., Siepmann, F., 2020. Sink conditions do not guarantee the absence of saturation effects. Int. J. Pharm. 577, 119009. https://doi.org/10.1016/j.ijpharm.2019.119009.

Costa, P., Sousa Lobo, J.M., 2001. Modeling and comparison of dissolution profiles. Eur. J. Pharm. Sci. 13, 123–133. https://doi.org/10.1016/S0928-0987(01)00095-1.

Siepmann, J., Peppas, N.A., 2001. Modeling of drug release from delivery systems based on hydroxypropyl methylcellulose (HPMC). Adv. Drug Deliv. Rev. 48, 139–157. https://doi.org/10.1016/S0169-409X(01)00112-0.

Karnik, I., Uttreja, P., Narala, N., Baisa, S., Elkanayati, R.M., Shawakri, E., Vemula, S.K., Repka, M.A., 2025. Twin-screw melt granulation of eudragit® FS100: optimization of coating-free delayed-release matrix tablets with HPMC K4M modulation. Int. J. Pharm. 686, 126325. https://doi.org/10.1016/j.ijpharm.2025.126325.

Lin, X., Ma, Q., Su, J., Wang, C., Kankala, R.K., Zeng, M., Lin, H., Zhou, S.-F., 2019. Dual-responsive alginate hydrogels for controlled release of therapeutics. Molecules 24, 2089. https://doi.org/10.3390/molecules24112089.

Pimton, P., Ratphibun, P., Tassaneesuwan, N., Chiangnoon, R., Uttayarat, P., 2022. Cytotoxicity evaluation of hydrogel sheet dressings fabricated by gamma irradiation: extract and semi-direct contact tests. Trends Sci. 19, 4583. https://doi.org/10.48048/tis.2022.4583.

Ma, S., Chen, M., Wang, Y., Wang, J., Hao, Y., Wang, X., Zhang, H., Wei, Y., Liang, Z., Hu, Y., et al., 2024. Gelatin-sodium alginate composite hydrogel doped with black phosphorus@ZnO heterojunction for cutaneous wound healing with antibacterial, immunomodulatory, and angiogenic properties. Int. J. Biol. Macromol. 274, 133456. https://doi.org/10.1016/j.ijbiomac.2024.133456.

Shao, J., Huang, H., Yu, J., Lan, X., Liu, W., Huang, Z., 2025. Multifunctional self-healing hemicellulose-based hydrogel for antimicrobial wound dressings and motion-responsive wearable sensing. Carbohydr. Polym. 370, 124364. https://doi.org/10.1016/j.carbpol.2025.124364.

Wiesmann, N., Mendler, S., Buhr, C.R., Ritz, U., Kämmerer, P.W., Brieger, J., 2021. Zinc oxide nanoparticles exhibit favorable properties to promote tissue integration of biomaterials. Biomedicines 9, 1462. https://doi.org/10.3390/biomedicines9101462.

Cai, X., Venkatesan, J.K., Schmitt, G., Reda, B., Cucchiarini, M., Hannig, M., Madry, H., 2023. Cytotoxic effects of different mouthwash solutions on primary human articular chondrocytes and normal human articular cartilage – an in vitro study. Clin. Oral Invest. 27, 4987–5000. https://doi.org/10.1007/s00784-023-05118-8.

Mattar, I., Landa, G., Frutos-Lizano, M., Izquierdo, N., Tapia, E., Perez, M., Lujan, L., Irusta, S., Mendoza, G., Arruebo, M., 2025. Multifunctional 3D-printed wound dressings containing a combination of synergistic antimicrobials in the management of MRSA infected topical wounds. ACS Appl. Mater. Interfaces 17, 47951–47968. https://doi.org/10.1021/acsami.5c08968.

Abdel-Rahman, R.M., Abdel-Mohsen, A.M., Frankova, J., Piana, F., Kalina, L., Gajdosova, V., Kapralkova, L., Thottappali, M.A., Jancar, J., 2024. Self-assembled hydrogel membranes with structurally tunable mechanical and biological properties. Biomacromolecules 25, 3449–3463. https://doi.org/10.1021/acs.biomac.4c00082.

Porrelli, D., Gruppuso, M., Vecchies, F., Marsich, E., Turco, G., 2021. Alginate bone scaffolds coated with a bioactive lactose modified chitosan for human dental pulp stem cells proliferation and differentiation. Carbohydr. Polym. 273, doi:10.1016/j.carbpol.2021.118610.

Zheng, Z., Qi, J., Hu, L., Ouyang, D., Wang, H., Sun, Q., Lin, L., You, L., Tang, B., 2022. A cannabidiol-containing alginate based hydrogel as novel multifunctional wound dressing for promoting wound healing. Biomater. Adv. 134, 112560. https://doi.org/10.1016/j.msec.2021.112560.

Chen, R., Salisbury, A., Percival, S.L., 2019. In vitro cellular viability studies on a concentrated surfactant-based wound dressing. Int. Wound J. 16, 703–712. https://doi.org/10.1111/iwj.13084.

Martin, V., Bettencourt, A.F., Fernandes, M.H., Alves, M.M., Hanafy, M., Cui, Z., Gomes, P.S., Santos, C., 2024. Green synthesis of Zn–Mg layered hydroxide nanoparticles with surface-mediated antioxidant and anti-inflammatory activity. Surf. Interfaces 46, 104037. https://doi.org/10.1016/j.surfin.2024.104037.

Tayyeb, J.Z., Guru, A., Kandaswamy, K., Jain, D., Manivannan, C., Mat, K.B., Shah, M.A., Arockiaraj, J., 2024. Synergistic effect of zinc oxide-cinnamic acid nanoparticles for wound healing management: in vitro and zebrafish model studies. BMC Biotech. 24, 78. https://doi.org/10.1186/s12896-024-00906-w.

Rakkan, T., Zhang, S., Lehner, S., Hufenus, R., Sangkharak, K., Ren, Q., 2024. Bio-based modification of polyhydroxyalkanoates (PHA) towards increased antimicrobial activities and reduced cytotoxicity. Int. J. Biol. Macromol. 275, 133132. https://doi.org/10.1016/j.ijbiomac.2024.133132.

Bar-Shai, N., Mann, D., Shalom, A., Nyska, A., Golberg, A., 2025. Biocompatibility and structural insights of seaweed-derived cellulose scaffolds in a subcutaneous implantation model. Sci. Rep. 15, 35667. https://doi.org/10.1038/s41598-025-19632-0.

Kumar, A., Sah, D.K., Khanna, K., Rai, Y., Yadav, A.K., Ansari, M.S., Bhatt, A.N., 2023. A calcium and zinc composite alginate hydrogel for pre-hospital hemostasis and wound care. Carbohydr. Polym. 299, 120186. https://doi.org/10.1016/j.carbpol.2022.120186.

Muller, G., Kramer, A., 2008. Biocompatibility index of antiseptic agents by parallel assessment of antimicrobial activity and cellular cytotoxicity. J. Antimicrob. Chemother. 61, 1281–1287. https://doi.org/10.1093/jac/dkn125.